Correlative non-destructive techniques to investigate aging and orientation effects in automotive Li-ion pouch cells

Fordham, Arthur; Milojevic, Zoran; Giles, Emily; Du, Wenjia; Owen, Rhodri; Michalik, Stefan; Chater, Phil; Das, Prodip; Attidekou, Pierrot; Lambert, Simon; Allan, Phoebe; Slater, Peter; Anderson, Paul; Jervis, Rhodri; Shearing, Paul; Brett, Dan

DOI:
10.1016/j.joule.2023.10.011

Document Version
Publisher's PDF, also known as Version of record

Citation for published version (Harvard):
Fordham, A, Milojevic, Z, Giles, E, Du, W, Owen, R, Michalik, S, Chater, P, Das, P, Attidekou, P, Lambert, S, Allan, P, Slater, P, Anderson, P, Jervis, R, Shearing, P & Brett, D 2023, 'Correlative non-destructive techniques to investigate aging and orientation effects in automotive Li-ion pouch cells', *Joule*, vol. 7, no. 11, pp. 2622-2652. https://doi.org/10.1016/j.joule.2023.10.011

Joule

CellPress
OPEN ACCESS

Article

Correlative non-destructive techniques to investigate aging and orientation effects in automotive Li-ion pouch cells

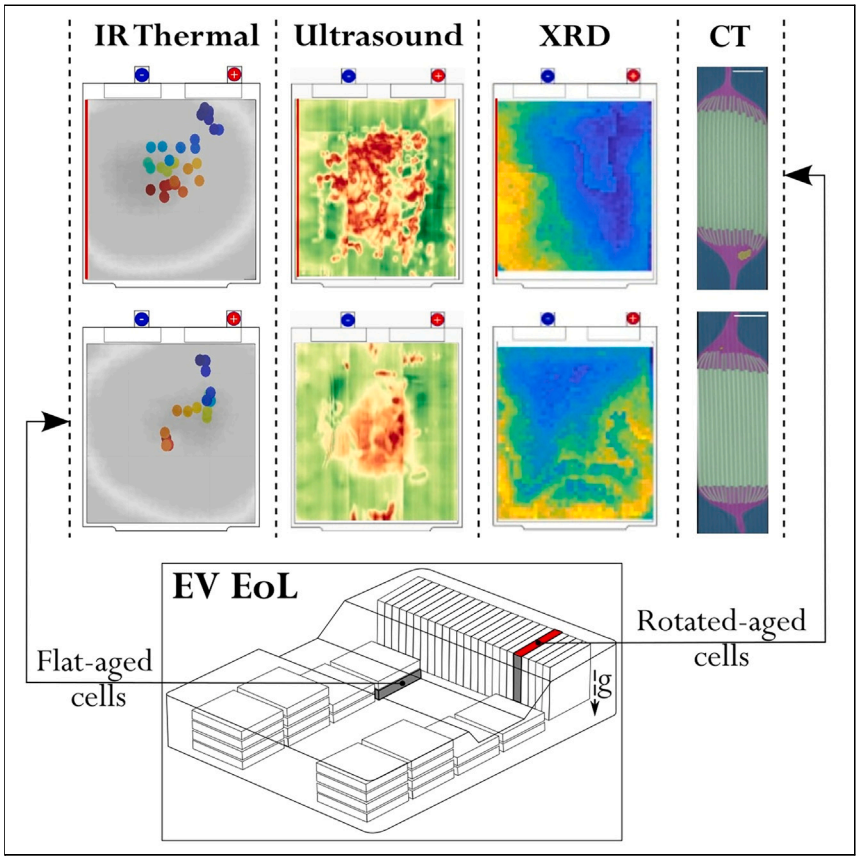

This study highlights the important impact of battery cell orientation and location on aging patterns within packs, offering vital insights for future pack designs. It pioneers four complementary characterization techniques, providing valuable information from simpler signals through correlation with more intricate synchrotron data. The research showcases the ability of cost-effective and accessible technology to match pricier methods for accurate state-of-health estimation. Ultimately, this work streamlines end-of-life cell decisions, optimizing performance, reducing raw material waste, and advancing sustainability in transport electrification.

Arthur Fordham, Zoran Milojevic, Emily Giles, ..., Rhodri Jervis, Paul R. Shearing, Dan J.L. Brett

paul.shearing@eng.ox.ac.uk (P.R.S.)
d.brett@ucl.ac.uk (D.J.L.B.)

Highlights

Cell orientation and location within a pack affect aging, informing future pack design

Employing four non-destructive techniques unlocked insight into EV cell degradation

SoH estimation by accessible technology can be as accurate as that by costly synchrotron

Enables efficient EoL cell decisions to optimize performance and reduce waste

Fordham et al., Joule 7, 2622–2652
November 15, 2023 Published by Elsevier Inc.
https://doi.org/10.1016/j.joule.2023.10.011

CellPress
OPEN ACCESS

Joule

Article

Correlative non-destructive techniques to investigate aging and orientation effects in automotive Li-ion pouch cells

Arthur Fordham,[1,2] Zoran Milojevic,[2,3] Emily Giles,[2,4] Wenjia Du,[1,2,6] Rhodri E. Owen,[1,2] Stefan Michalik,[5] Philip A. Chater,[5] Prodip K. Das,[2,3] Pierrot S. Attidekou,[3] Simon M. Lambert,[2,3] Phoebe K. Allan,[2,4] Peter R. Slater,[2,4] Paul A. Anderson,[2,4] Rhodri Jervis,[1,2] Paul R. Shearing,[1,2,6,7,*] and Dan J.L. Brett[1,2,*]

SUMMARY

The growing demand for electric vehicles (EVs) continues to raise concern for the disposal of lithium-ion batteries reaching their end of life (EoL). The cells inside EVs age differently depending on multiple factors. Yet, following extraction, there are significant challenges with characterizing degradation in cells that have been aged from real-world EV usage. We employed four non-destructive techniques—infrared thermography, ultrasonic mapping, X-ray tomography, and synchrotron X-ray diffraction—to analyze the aging of Nissan Leaf large-format pouch cells that were arranged in different orientations and locations within the pack. The combination of these methods provided complementary insights into cell degradation, with rotated/vertically aligned cells exhibiting distinct aging patterns compared with flat/horizontally aligned cells. These findings offer valuable information for pack design and demonstrate how cost-effective non-destructive techniques can provide practical assessment capabilities comparable to synchrotron studies. This approach enables decision support during EoL, enhancing battery production efficiency and minimizing material waste.

INTRODUCTION

The demand for lithium-ion batteries (LIBs) is increasing rapidly and will continue to do so in the decades to come to supply the growing requirement in modern society. In addition to increasing the rate of production, it is crucial to improve LIBs by enhancing power and energy density and extend the operating cycling lifetime in first-life applications. Currently, electric vehicle (EV) manufacturers consider a battery module within a pack to be at end of life (EoL) if it reaches 80% state of health (SoH). However, this decision tends to be based on limited or no knowledge of the SoH of individual cells. The individual cells inside the modules will have varying usage and thus SoH, depending on factors such as orientation, cooling system, and the location of the cell. A lack of information with respect to these factors often leads to some cells inside the pack being classified as at EoL when they have not fallen to 80% capacity, causing a wastage of raw materials, energy consumption, and time, with significant cost implications. This highlights the importance of diagnosing the defects of individual cells so that EV batteries can be reused in second-life applications and recycled only when EoL can be robustly determined. Numerous cell form factors are utilized within EV battery packs, such as pouch, cylindrical, and prismatic.

CONTEXT & SCALE

By 2030, all new vehicles will contain a battery pack. Manufacturers consider each module within a pack to be at end of life (EoL) when it reaches 80% state of health (SoH). These two factors will lead to a surge in used batteries.

Decisions on the recycling, reuse, or disposal of used batteries currently lack information on individual cell SoH. Therefore, we measured the aging of individual cells, extracted from different positions in a used vehicle battery pack, utilizing four different non-destructive techniques. We find that accessible, inexpensive technology can provide equally useful information for SoH estimation relative to costly synchrotron studies. The effects of orientation and location on the aging of the cell within the pack are illustrated by all techniques—useful for future battery pack design. Moreover, the results allow the decision on cell use at EoL to be made more quickly, optimizing the performance of these cells to help drive the sustainable electrification of transport.

Since packs contain different cell formats, it is important that the SoH measurements can be applied to each type. However, as demonstrated in Table S1 and Figure S1, pouch cells are one of the most used cell types for EVs, particularly those currently reaching the end of their life, and as such are the focus of this study.

Rapid diagnostic techniques are required for SoH optimization, both for determining the second-life use of cells and to provide pack designers with the relevant information to compare positions and degradation. These techniques need to be low cost, non-invasive, non-destructive, and rapid as well as effectively offer real-time *operando* prediction of the state of charge (SoC) and SoH. Ideally, the relevant methods should also be easily accessible and not, for example, require a synchrotron. These diagnostic approaches can work alongside electrochemical and crystallographic methods to help understand internal changes and defects occurring within cells.

Infrared (IR) thermography is a contactless and non-destructive technique that detects emitted radiation in the IR range of the electromagnetic spectrum. With known parameters, e.g., surface emissivity, camera distance, and reflected and atmospheric temperature, the temperature field of the measured object's surface can be determined with high spatial and temporal resolution. For pristine automotive pouch cells, the technique is mostly used for the validation of electrochemical-thermal[1,2] and electro-thermal[3,4] models with experimentally obtained cell surface temperatures during cycling.

Different cell orientations and tab positions can result in a heterogeneous distribution of the SoC,[5] current densities, and voltage, which can cause temperature gradients across the battery.[6,7] As battery performance is strongly linked to temperature,[8] temperature gradients will influence aging mechanisms during long-term usage.[9] Battery aging characterization by IR thermography has been covered in several studies. Veth et al.[10] highlighted the possibility of *ex situ* IR thermography characterization of large-format pouch cells (high/low current cycled and calendar aged) that have been aged to different degrees. In-plane aging non-uniformities, across the surface of the cell, and *real* EoL detection in battery second-life application by temperature derivative map analysis are presented.[11] Robinson et al.[12] used IR thermography to detect internal defects (gas pockets formed during cell aging) using "lock-in" thermography. The influence of different orientations on in-plane temperature derivative maps for pristine and EV life-aged large-format pouch cells are presented in a previous work by Milojevic et al.[13] IR thermography is well suited to large-format pouch-cell measurements because of the flat geometry and can be a useful tool for battery manufacturers to minimize expected thermal/aging gradients in the battery design stage and for in-plane aging characterization.

Ultrasonic testing is an acoustic technique that involves an externally generated signal produced from a piezoelectric transducer in contact with a cell.[14] This signal is propagated through the material before being recorded either by the same transducer via the reflection of the signal in the material or another transducer attached to the opposite surface of the cell. The technique allows the analysis of the internal structure of the system because acoustic wave propagation is affected by the condition of the battery material. For further details on ultrasound testing, the reader is directed to recently published reviews by Majasan et al.[14] and Popp et al.[15] as well as earlier work by Hsieh et al.,[16] Chang et al.,[17] Bommier et al.,[18] Sood et al.,[19] and Gold et al.[20]

The initial application of ultrasound to batteries focused on fixed-point testing, which cannot probe heterogeneity across the entire Li-ion cell. Robinson et al.[21]

[1]Electrochemical Innovation Laboratory, Department of Chemical Engineering, University College London, London WC1E 7JE, UK

[2]The Faraday Institution, Quad One, Harwell Science and Innovation Campus, Didcot OX11 0RA, UK

[3]School of Engineering, Newcastle University, Newcastle upon Tyne NE1 7RU, UK

[4]School of Chemistry, University of Birmingham, Birmingham B15 2TT, UK

[5]Diamond Light Source Ltd., Harwell Science and Innovation Campus, Didcot OX11 0DE, UK

[6]ZERO Institute, University of Oxford, Holywell House, Osney Mead, Oxford OX2 0ES, UK

[7]Lead contact

*Correspondence: paul.shearing@eng.ox.ac.uk (P.R.S.), d.brett@ucl.ac.uk (D.J.L.B.)

https://doi.org/10.1016/j.joule.2023.10.011

were the first to report spatially resolved mapping using ultrasonic time-of-flight (ToF) analysis at 36 positions in a mobile-phone battery to identify inhomogeneities throughout the cell. They were able to distinguish the depth of the defect as well as determine that changes in signal amplitude correlated to the degree of lithiation of the respective electrodes. It was found that the ToF of the signal decreased with an increased SoC. Robinson et al.[22] then produced 12 lab-made Li-ion cells with purpose-built defects and used ToF mapping to identify their presence. The acoustic scans could locate the depth of defect within the cell, and this was confirmed using X-ray computed tomography (CT) scans.

Other examples of ultrasonic mapping have observed electrolyte wetting in Li-ion pouch cells.[23] It was found that ultrasonic images of fresh and aged cells with different cycling conditions exhibit very different ultrasonic transmittance. This means that it can be used to probe structural defects and failure mechanisms within cells, such as electrolyte drying. In Deng's arrangement, the ultrasonic pulse was transmitted from one transducer and received from another on either side of the cell (transmission mode). The sensor had a diameter of less than 1 mm that allowed relatively high-resolution mapping and was able to determine the state of electrolyte and/or gas within a cell. Gauthier et al.[24] used ultrasonic transmission mapping (UTM) to determine how the depth of discharge (DoD), C-rate, and age affect capacity retention and the impedance of pouch cells cycled for 20,000 h. The results showed that poor ultrasonic transmission arises when the wetting of the electrolyte does not occur in the pore spaces in the electrodes.

Although the works of Deng et al.[23] and Robinson et al.[21,22] produced abundant information about the internal structure of batteries, ultrasound mapping has principally been performed on small-format cells,[25–28] with the exception of a recent work by Xie et al.,[29] who used ultrasonic techniques for non-automotive large-format cells. Therefore, the research in this paper is the first to demonstrate the value of acoustic mapping on large-format cells that have been aged in EVs and the value of the technique for use in manufacturing and industry. Moreover, it is the first time that multiple cells from a pack and the influence of cell orientation have been examined for large-size pouch LIBs using ultrasound mapping.

Over the last decade, X-ray CT has been widely used to non-destructively characterize the 3D structure of electrochemical materials and energy storage devices across multiple length and time scales.[30,31] Lu et al.[31] employed nano-CT (126-nm voxel size) to reveal the structural heterogeneities formed under high C-rate cycling. The microstructural evolution of Si particles was captured using the high-speed synchrotron micro-CT by Taiwo et al.,[32] and the cracking propagation and fracturing were tracked in real time during the early stages of lithiation. These investigations at the nanoscale and microscale (from the particle to electrode level) have facilitated cell engineering, such as the development of new electrodes, by understanding the role of materials' structure in electrode degradation. Additionally, the advantages of macro-CT include its higher power output and larger experimental chamber, allowing for bigger samples in industrial applications.[33,34] At the cell level, extensive work has been undertaken to image cylindrical-type Li-ion cells using X-ray CT[35–38] to determine deformation in electrode architecture, and multimodal characterization has been used to provide a comprehensive understanding of 18650 cell aging.[37]

To date, macro-CT studies of pouch-type cells are very limited. Bond et al.[39] observed electrolyte depletion as a function of SoC. Du et al.[40] showed that cycle-induced gas generation could be tracked in a Li-ion pouch cell (400 mAh) by

mapping the thickness evolution in 4D. Shateri and co-workers illustrated the effect of aging temperature on macrostructure using 19 Ah Li-S prototype pouch cells.[41] However, there is a need to characterize Li-ion pouch cells with high energy (up to 30 Ah per cell) and large size (up to hundreds of mm) dissembled from used EV modules to help determine the most appropriate forward processing and use (i.e., reuse, recycling, recovery, or disposal).[42] This requirement is based on the following. First, there is a lack of information in the open literature. Second, scanning pouch cells is more challenging than cylindrical cells because of the high aspect ratio (the laterally extended pouches, whose sizes are much larger than the detector's effective field of view, lead to difficulty in imaging the whole projection dataset of inner structures because of inadequate X-ray transmission in the extended direction). Third, pouch-type cells are a major battery format and enable a higher pack-level energy density than cylindrical-type cells due to improved space utilization. Fourth, there is an impending challenge of dealing with a huge number of spent battery packs by 2030. Fast macro-CT scans could play a crucial role in evaluating the SoH for the second-life application. Fifth, different battery cell sizes and configurations can have different fault and degradation mechanisms.[35,43] Finally, studying cells disassembled from used EV battery packs requires multiple expertise, including mechanical, electrical, and electrochemical expertise.

X-ray diffraction (XRD) gives information about the crystallographic structure and composition of a material. Compared with lab-based sources, synchrotron X-rays are of higher intensity, are of tunable energy and beam size, and produce higher-resolution diffraction patterns with improved signal-to-noise ratios. This allows for rapid data collection, enabling *in situ* processes to be studied, with high-energy incident beams able to pass through a range of sample environments. In battery research, *in situ* and *operando* studies using specially designed cells have been performed to elucidate structural and compositional changes during cycling and monitor solid electrolyte interphase (SEI) formation and the evolution of strain within electrodes.[44] Long-duration experiments, where XRD data are collected periodically over the lifetime of the cell, have enabled the long-term degradation of battery materials to be studied.[45] One such study on long-duration degradation by Leach et al.[5] collected XRD data across nine sites on a single-layer small-format NMC811/graphite pouch cell over 900 cycles. They found that the SoC of the edges and corners of the pouch cell increased slower than the center of the cell on charging and contained a greater proportion of a fatigued phase. The authors speculated that these spatial inhomogeneities may become more pronounced in larger-format pouch cells or cylindrical cells.

Synchrotron XRD has been used to map the spatial inhomogeneities within $LiNi_{0.6}Mn_{0.2}Co_{0.2}O_2$ (NMC622)/Li pouch cells, with the technique termed high-energy lateral mapping (HELM).[46] Mattei et al.[46] tested two samples using HELM. They lab assembled a seven-layer pouch cell in pristine condition and a single cathode layer taken from an equivalent cell that had been aged by constant current constant voltage (CCCV) cycles in the lab (as opposed to aged in real-world application) to 10% of its initial discharge capacity. In the pristine pouch cell, two parameters were mapped, the loading level and unit cell volume of NMC622, and were both found to be homogeneous across the entire area of the cell. The only exception was a substantial excess of NMC622 present on the sample tab. The single-layer cathode sheet possessed a few "hotspots" where the cathode material was of higher SoC (inferred from the unit cell volume) and of lower abundance. On closer inspection, a second NMC622 phase of higher SoC coexisted within these hotspots with a primary phase that had the same SoC as the rest of the cell. HELM (or high-energy

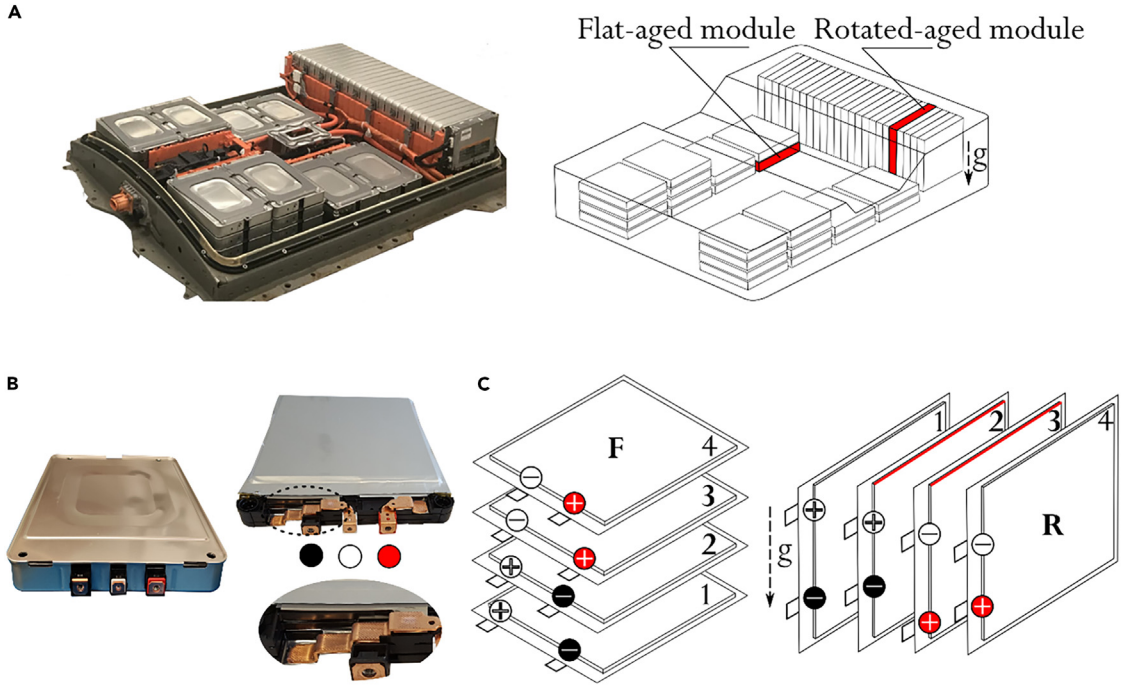

Figure 1. Battery pack configuration, module variations, and cell locations of those used in the investigation

(A) Battery pack and position of the tested modules in the pack.

(B) Module with casing (left), without casing, and busbar-tab connections in the module and gravity vector direction (right).

(C) Positions of the tested cells (2 and 3) in the module and their orientations in the pack (F, flat; R, rotated aged); for rotated-aged cells, edges opposite to the gravity vector are marked with the red lines.

XRD [HEXRD]) has been used to spatially map Li plating, the extent of the lithiation of the graphite anode, and the cathode SoC in a single-layer NMC532/graphite pouch cell.[47]

This paper explores the value of multimodal, non-destructive diagnostic techniques, including thermal imaging, ultrasound mapping, X-ray CT, and synchrotron XRD, to examine five large-format multi-layer Li-ion Nissan Leaf cells that were positioned in different orientations and locations within a used vehicle battery pack. Applying this combination of techniques to cells of this large size, which have been aged in real-world conditions, is a novel approach. These techniques demonstrate differences in the homogeneity of aging across cells and the importance of cell orientation and location within the pack. Insights into future battery pack design by demonstrating which cell orientations will optimize performance and minimize degradation across all cells, as well as improvements to recycling strategies for EoL cells, can be drawn from the study. Although the focus of this work is on pouch cells, each of the techniques may also be combined and applied to other formats such as cylindrical cells.

RESULTS

Battery specification

Experiments were carried out on automotive large-format pouch cells (blended cathode consisting of lithium manganese oxide [LMO] with lithium nickel-cobalt-aluminum oxide [NCA] and graphite anode) extracted from two first-generation Nissan Leaf battery modules.[48] These pouch cells have a capacity of 32 Ah and dimensions of 261 × 216 × 7.91 mm and consist of 17 double-sided cathode sheets and 18 double-sided anode sheets. The battery pack contains 48 passive cooled

modules (Figure 1A) arranged in two side stacks (2 × 12 modules) and one rear stack (1 × 24 modules). The passive cooling system used in first-generation Nissan Leaf battery packs gives rise to small temperature differences across the cells in the module. Modules from the rear stack were more likely to experience slightly higher temperatures during operation compared with the modules on the sides. Active cooling would provide dynamic thermal control, which in general should reduce these small temperature differences. Nonetheless, the temperature differences observed in passive cooling are not substantial and would not be expected to substantively influence the degradative behavior. Before the modules were removed from the EV, battery management system statistics showed the battery pack's SoH to be 76.96%, where SoH throughout the paper refers to the capacity fade of indivdual cells extracted from within the pack. For this study, two modules with different orientations in the battery pack (Figure 1A, right) were disassembled to the cell level. In each module, four batteries (labeled 1–4 from the bottom of the module) are connected in 2P × 2S arrangement, and to establish a connection with busbars, cell tabs were cut during manufacturing depending on the position in the module (Figure 1B). For analysis in this study, two middle cells (number 2 and number 3) from selected modules were tested and compared, and their orientations in the pack are shown in Figure 1C (flat-aged modules [F] and rotated-aged modules [R]).

Although the total disassembly of a battery pack in this way can be time-consuming, automated methods are currently being developed to increase its speed and safety, maximizing potential returns from reuse. If a complete disassembly of the pack in this manner is not possible, analyzing individual cells in several packs can still provide valuable information about pack design and reveal where cells in a pack become more degraded during use. This information can aid in future module level disassembly and use, making the process more efficient and effective. For comparison with the aged cells, a pristine cell was also investigated, the results of which are provided in ultrasound measurements and X-ray CT measurements. The pristine cell was obtained from a second-generation Nissan Leaf battery with a cathode consisting of $LiNi_{0.5}Mn_{0.3}Co_{0.2}O_2$ (NMC532). The dimensions were the same as first-generation cells. Although the chemistry differs from the first-generation aged cells, it is expected that the lack of degradation will be evident and, therefore, provide a suitable comparison. Each cell was discharged to 3 V for all measurements unless otherwise stated.

IR thermal measurements

Thermal imaging was performed during the discharge step of cell cycling, and the results are presented in two sections. The first section covers obtained lumped parameter results (capacities and mean temperatures relative to the initial cell temperature [T_{Mean}]), whereas the second section covers the spatial thermal behavior of the cells.

Lumped parameters

An example of the test procedure used for each of these tests and a typical voltage profile are shown in Figure 2A. Figure 2B depicts the voltage versus capacity graphs obtained during the thermal imaging discharging cycle for the four batteries investigated. Mean relative temperature profiles during discharging for all batteries are shown in Figure 2C. Measured cell capacities (Q) and mean relative temperatures (T_{Mean}) at the end of discharge are displayed in Table 1.

In Table 1, it can be seen that higher capacities are measured for flat-aged batteries (F2 and F3, 28.6 and 28.2 Ah, respectively), whereas lower capacities are measured

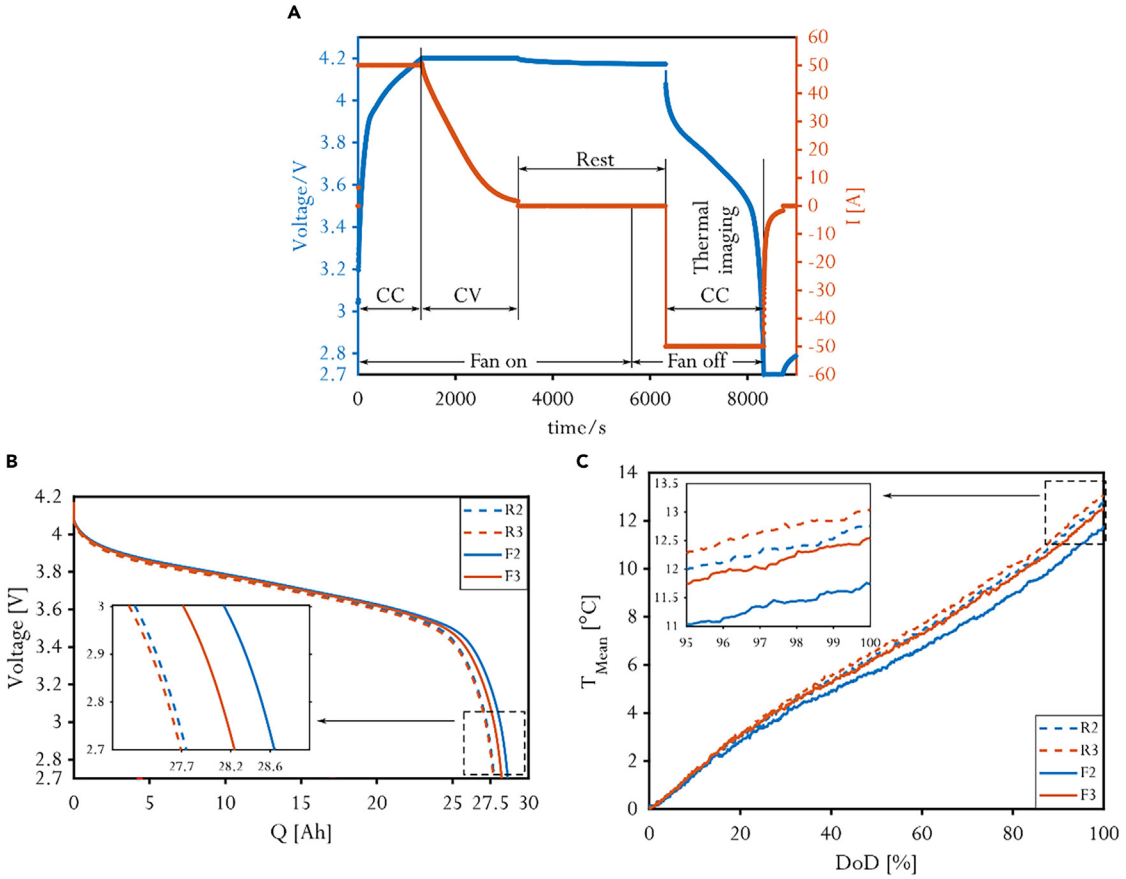

Figure 2. Procedure for thermal imaging measurements during electrochemical cycling and associated performance metrics

(A) Thermal imaging cycling procedure: constant current charging (CC) at 50 A and 4.2 V constant voltage (CV) until the current dropped to less than C/20 followed by a 1-h rest period. Thermal imaging was performed during CC discharge at 50 A until the voltage reached 2.7 V with the environmental chamber turned off.

(B) Voltage versus capacity measured during thermal imaging discharging cycle.

(C) Mean relative temperatures T_{Mean} recorded during thermal imaging.

for rotated-aged batteries (R2 and R3, 27.8 and 27.7 Ah, respectively). The maximum capacity-based SoH difference is 2.8%. $T_{RelMean}$ at the end of discharge is in good correlation with the measured capacities, where batteries with lower capacities reached higher temperatures compared with batteries with higher measured capacities. Further electrochemical measurements highlighting the disparity between the cells are shown in Figure S3 as well as in a previously reported work by Milojevic et al. [13]

Spatial variation of temperature

Although previously presented average results show that rotated-aged batteries have lower capacities and higher temperatures at the end of discharge (see Table 1), the temperature maps were further processed in two ways to investigate the spatial aging difference between flat- and rotated-aged batteries. First, the position of the maximum relative (increased) temperature (T_{RelMax}) over the course of discharge was tracked and extracted at every second in the DoD range to generate the hotspot map shown in Figure 3A; here, the DoD of each point is indicated using a color scale. Second, the position of the maximum temperature derivative (dT/dt) was calculated and tracked over the course of discharge to generate the hotspot map shown in

Table 1. Measured capacity (Q) and mean relative (increased) ($T_{RelMean}$) temperatures at the end of discharge for the tested cells

	New	F2	F3	R2	R3
Q (Ah)	32.5	28.6	28.2	27.8	27.7
SoH (%)	100	88.0	86.8	85.5	85.2
$T_{RelMean}$ (°C)	–	11.7	12.5	12.8	13.0

Figure 3B, where the DoD is indicated using the color scale. The dT/dt measurements give an indication of where the biggest temperature changes are occurring each second. The T_{RelMax} provides an indication of where the majority of the heat-generating activity has been occurring, whereas the *dT/dt* measurements give information about where the largest changes in heat-generating activity are occurring at that point in time, regardless of whether it is the highest temperature across the surface of the cell at that point. Both sets of results are also shown in Video S1. The spatial variation of the temperature rise as a function of DoD is displayed in this video.

Figure 3 indicates that hotspot positions extracted from T_{Rel} maps (Figure 3A, top) are influenced by the geometry of the tabs, especially at the beginning of discharge (at low DoD). At low DoD, hotspot positions are closer to the positive tab for cells F3 and R3, whereas for F2 and R2, they are closer to the negative tab. For the rotated cells, this position is closest to the edge oriented downward. As DoD increases, the position of the hotspots shift toward the center of the cell for all cells. The T_{RelMax} hotspot position can be associated to the area of the cell undergoing most electrochemical activity and resistance, causing a higher temperature. For all cells, the T_{RelMax} hotspot never drops below the center of the cell throughout the whole discharge, implying that cell usage is greatest near the respective tabs at the start of DoD and then shifts to the center at high DoD. R3 and F3 cells reached slightly higher T_{RelMax} values at the end of discharge compared with R2 and F2 (Figure 3A, bottom).

Hotspot positions extracted from *dT/dt* maps show different behavior. Values of the hotspots (dT/dt_{Max} in Figure 3B, bottom) for rotated-aged cells (R2 and R3) are higher compared with the flat-aged cells (F2 and F3). This increased temperature suggests that rotated cells underwent greater stress and resistance during discharge compared with the flat ones, leading to greater aging after long-term cycling. These results are in good correlation with the measured capacities presented in Table 1. The hotspot positions extracted from *dT/dt* maps (Figure 3B, top) provide more interesting results. At the beginning of discharge (<20% DoD), dT/dt_{Max} hotspot positions are similar and are aligned between the tabs. This result differs compared with T_{RelMax} positions (Figure 3A, top) at the same low DoD. As DoD increases, the flat-aged cells' (F2 and F3) dT/dt_{Max} hotspots shift in a similar direction toward the center. In contrast, the rotated-aged cells' (R2 and R3) hotspot shift is less uniform. Between 20% and 60% DoD, there is movement of hotspot position to the side of the cell that was oriented upward, as illustrated in Figure 1C. For R2, this direction was to the positive tab, and for R3, it was to the negative tab. From 80% to 100% DoD, the hotspot position shifts toward the center. For R2, there is greatest dT/dt_{Max} shift toward the bottom of the cell, which is not seen in R3 or the flat cells.

Ultrasound measurements

The ultrasonic mapping results are dependent on the amplitude and ToF of the signal as it passes through the battery material. The amplitude of the signal is

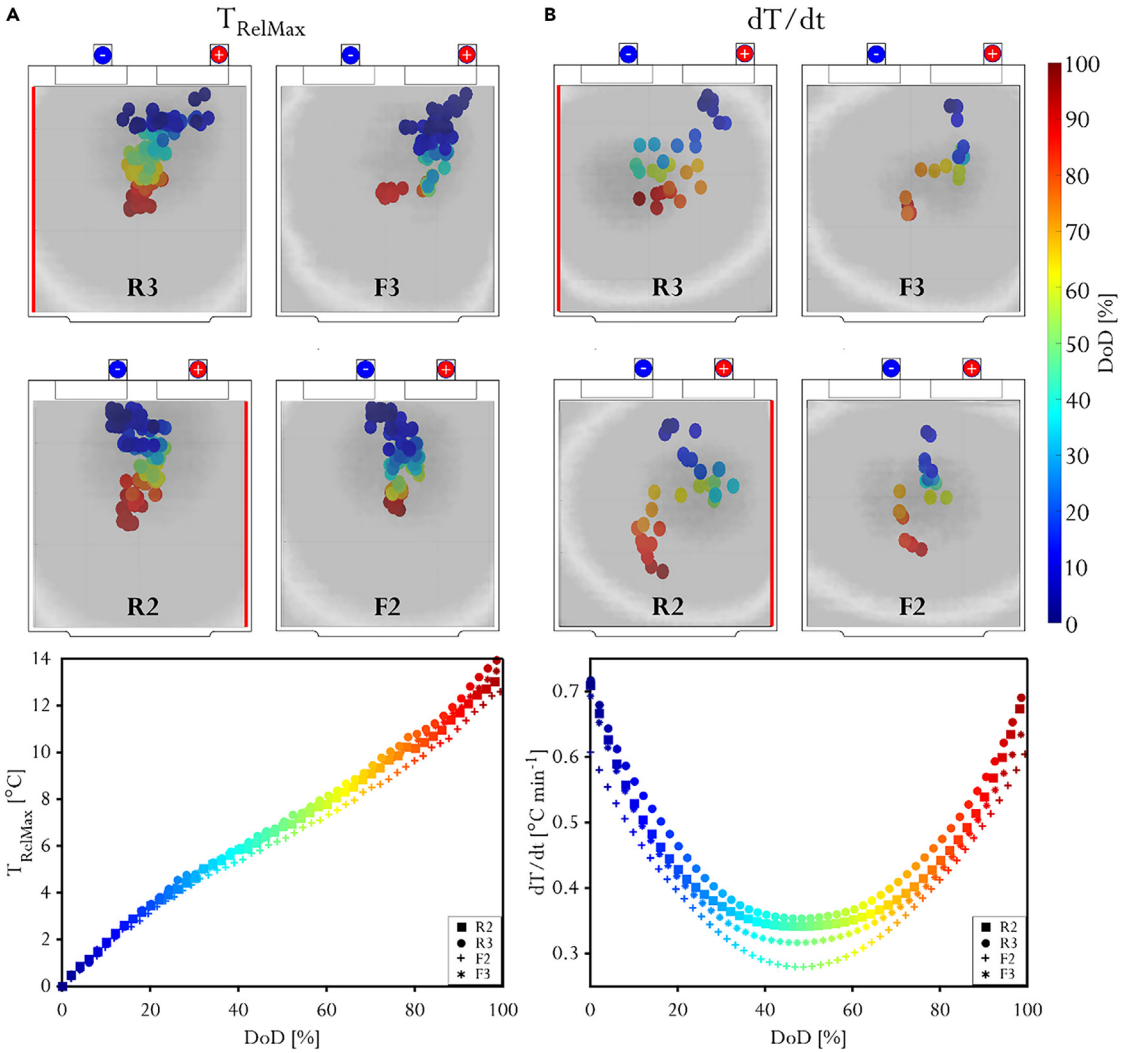

Figure 3. Thermal imaging results for each cell investigated

(A) Hotspot maps showing the changing position of maximum relative (increased) temperature T_{RelMax} over the course of discharge for each of the four cells.

(B) Hotspot maps showing the changing position of the maximum *dT/dt* during the course of discharge. Depth of discharge for each of the points is shown in using the color scale. Plots showing how T_{RelMax} and maximum *dT/dt* are shown below the images. Maps (in gray) over the surfaces present T_{Rel} (A) and *dT/dt* (B) at 40% depth of discharge. For rotated cells, the edges oriented upward are marked with red lines to illustrate the effect of gravity. The gravity vector is displayed in Figure 1C.

affected by the medium through which it passes. The wave will be attenuated by changes in the internal structure of the cell. As the cell ages, changes occur in the layers of the cell structure, the electrolyte distribution, and gas that is generated. An ultrasonic signal passing through wetted electrolyte is attenuated far less than that traveling through an "unwetted" section where the electrolyte has been consumed and dried up. For a "dry" electrode, the ultrasonic signal can only transmit between particles inside the internal structure. These particles are at different orientations and shapes causing reflection and scattering, leaving the acoustic signal greatly attenuated. However, for the wetted areas, the electrolyte acts as a medium for the ultrasonic signal to transmit, allowing the wave to propagate with minimal attenuation.

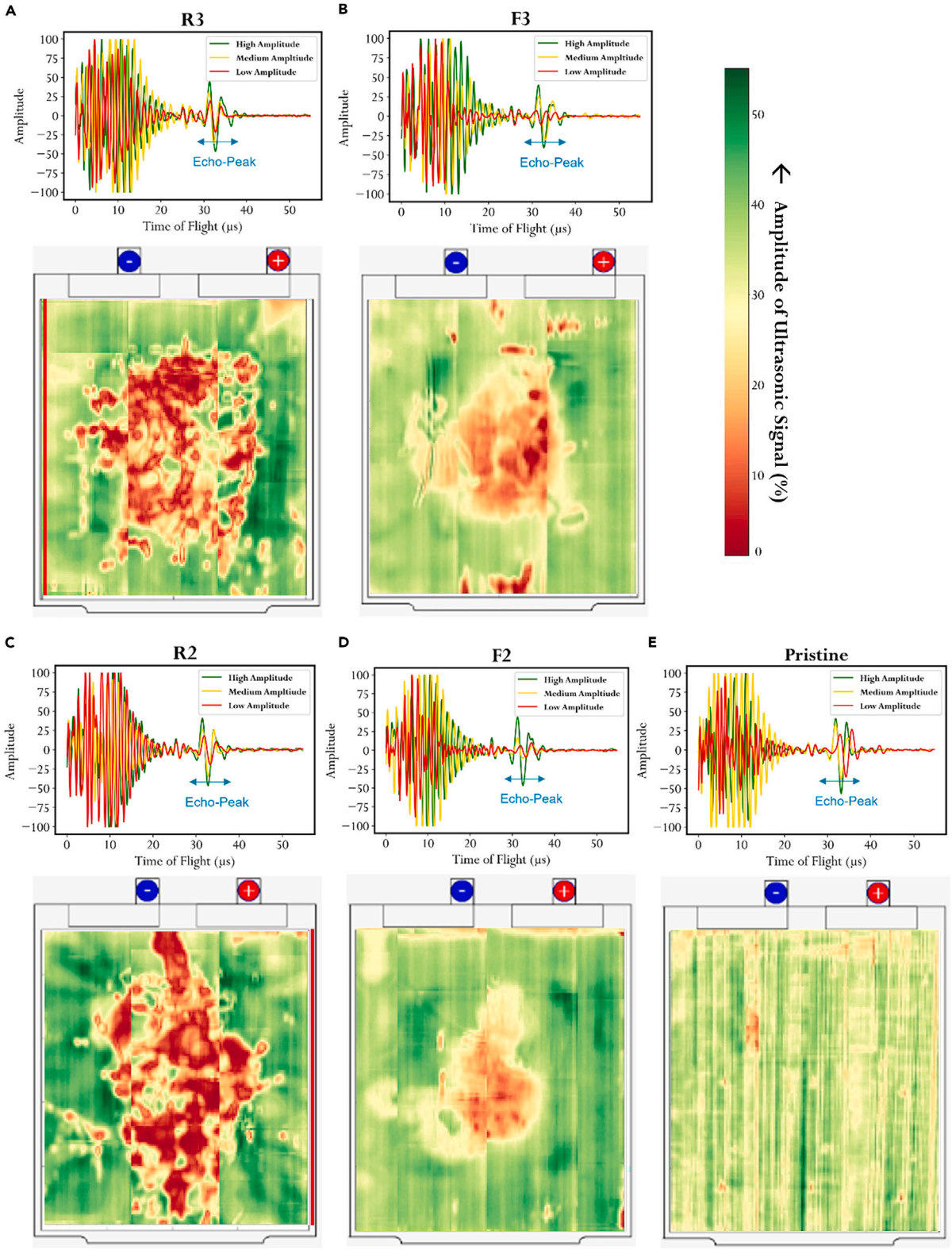

Figure 4. Ultrasound acoustic mapping results for each cell investigated

The waveform plot displays three separate signals overlayed for different parts of the cell. The green line indicates an area of high signal amplitude, indicating that it has been attenuated least. The red line indicates an area where the signal has been most attenuated and hence has the smallest

Figure 4. *Continued*
amplitude, whereas the yellow waveform is in an area where the signal is dampened an amount in between the two. The color maps represent the amplitude in the chosen gate (blue arrow) across every point in the cell. (A) R3 and (C) R2 are cells of rotated orientation inside the battery pack. (E) Pristine is a cell before it has been cycled inside a pack. (B) F3 (D) F2 are cells of flat orientation inside the battery pack. The scale shows the peak amplitude represented as a percentage of the most intense positive and negative peaks (0 is the smallest amplitude [red], and the highest amplitude is green). For rotated cells, the edges oriented upward are marked with thicker red straight lines to illustrate the effect of gravity.

The amplitude and ToF of the ultrasonic signal will also be affected by changes to the internal structure induced by cycling and aging. The speed of the ultrasonic wave, c, through the cell is related to Young's modulus, E, and density, ρ (see Equations 1 and 2):

$$v = \sqrt{\frac{E}{\rho}} \quad \text{(Equation 1)}$$

$$ToF = \frac{L}{v} = \frac{L}{\sqrt{\frac{E}{\rho}}} \quad \text{(Equation 2)}$$

ToF thus increases with the distance the signal travels, L, and with increasing density and decreases with growing elastic moduli. The signal travels faster through a medium with greater elastic modulus. For these investigations, it was found that electrolyte depletion had a bigger impact on the amplitude of the signal than the ToF; thus, we focused on amplitude measurements rather than ToF. Although out of the scope of this study, ToF measurements can provide additional insights into degradation and other related information. Moreover, using the fundamental Equations 1 and 2, one could calculate well-defined moduli values for the electrodes as done by Chang et al.[17] by using CT to determine the accurate thickness of electrodes and considering the complex electrode heterogeneity. Here, we do not have high enough resolution CT data due to the large-size cells used in the study. Nonetheless, this method is a valuable tool for future work.

Figure 4 displays the results of the ultrasound mapping measurements for each cell. Color maps for each cell are shown, with the red end of the spectrum representing higher signal attenuation (lower amplitude) and the green end indicating a more intense signal (higher amplitude). The amplitude is not normalized across all scans, meaning that colors on different cells can be directly compared. A waveform plot indicating how the signal changes across the surface of the cell is included above each color map. Color maps are generated based on the amplitude of the signal in the chosen gate, over a ToF range of 26–38 μs, and this region was chosen because it contains the "first echo" peak. A first echo-peak is generated by the signal that has traveled through the whole cell before being reflected. This signal is analyzed since it gives information about the entire internal structure of the cell.

In the flat (F2 and F3) cells, the darker red and yellow areas are present in a central uniform position, indicating low-amplitude signals. F3 has more areas where the signal has been attenuated relative to F2, but both occur in similar positions. The edges have very few red areas, implying that the signal has passed through at high amplitude. In contrast, rotated cells (R2 and R3) have far more areas of high attenuation, spread in a non-uniform position across the whole cell. For R3, the positive tab was oriented lowest, relative to the bottom of the battery pack, and the low-amplitude signal appears to be seen across both sides of the cell. For R2, the negative tab was oriented lowest, and the red, low-amplitude area stretched across the whole middle of the cell and toward the positive tab. The different

Table 2. Percentage areas of high acoustic attenuation in each cell calculated using image processing

	Pristine	F2	F3	R2	R3
Percentage area of high acoustic attenuation (%)	0.58	6.36	12.6	24.3	21.5

patterns seen in the color maps appear to be dependent on cell orientation. An image processing method, outlined in X-ray CT and image processing, was used to spatially quantify the distribution of the acoustic attenuation in nine sub-sections of each cell. These images are displayed in Figure S6. The results found the sub-sections with highest percentages of acoustic attenuation in the rotated cells, particularly the sub-sections closest to the upward edge. This phenomenon was most notable for R2, which had a 32% area of high attenuation on the upward edge compared with 24% in the sub-section containing the edge oriented downward. For reference, a pristine second-generation Nissan Leaf pouch cell was also scanned using ultrasound ToF measurements. Although this cell is of a different chemistry, the new, non-aged nature of the cell is expected to be representative of a fresh first-generation Nissan Leaf cell that has not been subjected to uneven stresses resulting in degradation. In the center, there is no area of low-amplitude signal as in the aged cells, with a uniform acoustic signal generated across the surface of the cell. Relative to the aged cells, the waveform plot for the pristine cell displayed the highest-amplitude signal, within the echo-peak range. Slight striations in the data are likely caused by the movement of the sensor array required to cover the large area of the cell.

The same image processing method was also used to quantify the overall fraction of the most degraded areas across each cell. As seen in Table 2, the pristine cell, expected to have a completely uniform structure before cycling, displayed a fraction of differing color of 0.58%, confirming the hypothesis. The rotated cells, R2 and R3, contained a far greater fraction of degradation than the flat cells, F2 and F3. The similar fraction of ~25% for each of the rotated cells confirms the consistent negative effect of this orientation on SoH and correlates to the similar SoH values seen in Table 2. The flat cells show a fraction that is far less than the rotated cells with F2 less than F3. The SoH and capacity of F2 are recorded as slightly higher than those of F3, which matches the results seen in the image processing of the ultrasound data, further emphasizing the success of acoustic techniques as a quantitative diagnostic method.

X-ray CT measurements

The acoustic technique is regarded as a low-cost and rapid probe to identify the initial gas distribution and other defects within a pouch cell.[40] The previous section showed that Li-ion cells, operated in different orientations inside the pack, displayed distinct variations in their associated acoustic maps, thought to be associated with areas of internal cell degradation. Macro-CT scans were performed on the representative samples at the corner opposite to the tabs, namely pristine, flat-aged (F2 and F3), and rotated-aged (R2 and R3) samples. A lab-based CT scanner, with a spatial resolution of 45 μm pixel size, was employed to complete and validate the prior acoustic results by providing architecture information in 3D at the cell level. To better observe and quantify the multi-class features in each sample, the trained U-net 3D model was applied to segment these 16-bit grayscale images, and the results (Figures 5 and 6) demonstrate that the deep learning-assisted segmentation tool has a valuable role in battery analysis by X-ray imaging.

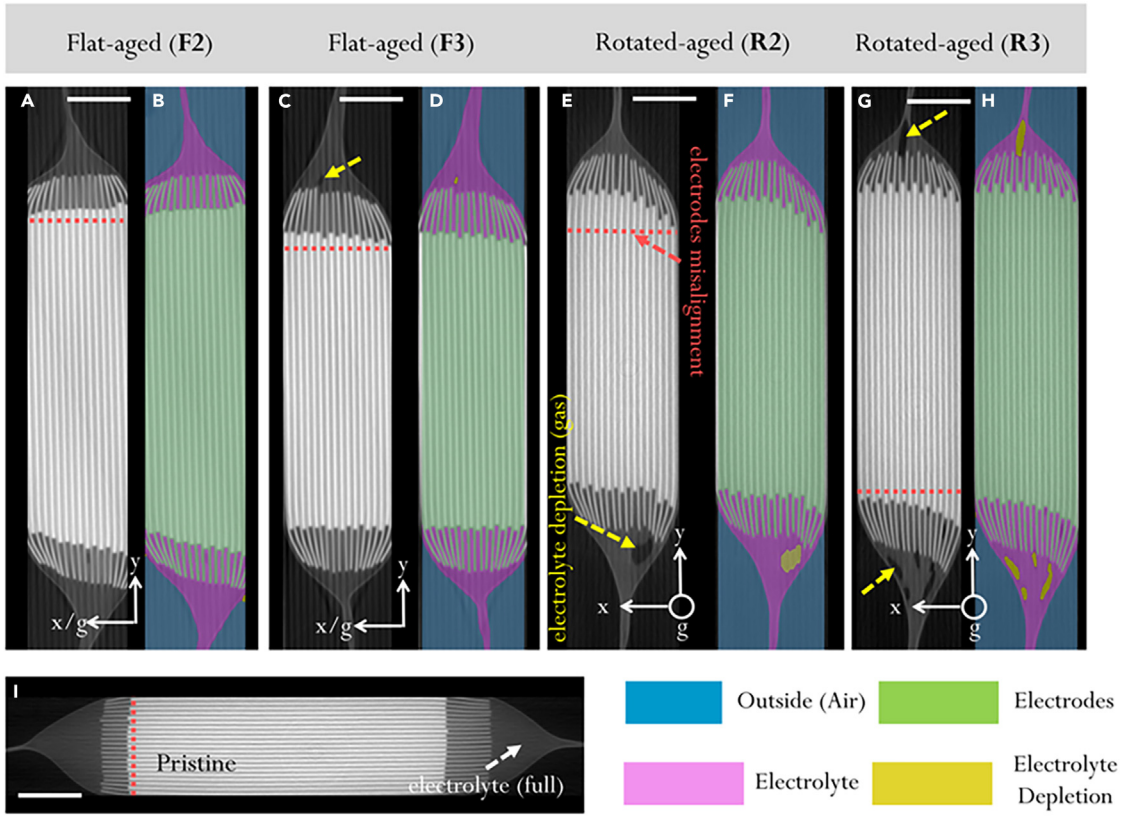

Figure 5. X-ray CT results for each cell with deep-learning-assisted segmentation

Tomographic slices of large Li-ion pouch cells at the corner opposite to the tabs under the status of (A–D) flat aged, (E–H) rotated aged, and (I) pristine, showing the overall macrostructure under the two different placements. The side views (x-y plane) are extracted from the region of interest (ROI) volumes. The pink arrows highlight the low X-ray attenuation zones (black area because almost no loss of X-ray photons), indicating the electrolyte loss after aging, in particular for the rotated-aged (R2 and R3) samples. The red dashed lines are drawn to indicate the alignment of the electrode layers, suggesting that the rotated samples have the highest misalignments among all samples. The trained U-net model was applied to the greyscale images (A, C, E, and G), demonstrating deep-learning-assisted segmentation (B, D, F, and H) of four labeled phases (blue: outside; green: electrodes and separators; pink: electrolyte; and yellow: electrolyte depletion). The white scale bars represent 4 mm for all figures. The coordinates are labeled along with the direction of gravity, g.

In Figure 5, 2D longitudinal slices taken from the corners (Figure S5) of three large Li-ion pouch cells are presented. The same measurements were performed for each corner and showed similar results, but for clarity, only the bottom right corner opposite to the positive tab is displayed in this paper. Although the nature of geometric limitation (high aspect ratio) restricts further high-resolution acquisitions, it is sufficient to obtain the typical parallel-layer structures. Higher density materials will have a brighter phase in the X-ray image because of high X-ray attenuation, and vice versa. In these side views at the x-y plane, the electrodes (both anode and cathodes), electrolyte, separators, and some defects were resolved based on their density.

Figure 5I demonstrates the non-defects in the pristine cell. It is important to note that the pristine Nissan Leaf cell is a second-generation design containing more structural layers than the other first-generation aged cells analyzed and a different chemistry.[49] Nonetheless, the X-ray CT result confirms that the electrode layers are better aligned, and the electrolyte is fully wetted. Clearly, the rotated-aged cells (Figures 5E–5H) have the most prominent electrode misalignment compared with flat-aged (Figures 5A–5D) and pristine (Figure 5I) cells. This observation is confirmed by drawing a red dashed line perpendicular to the electrode layers, showing that the

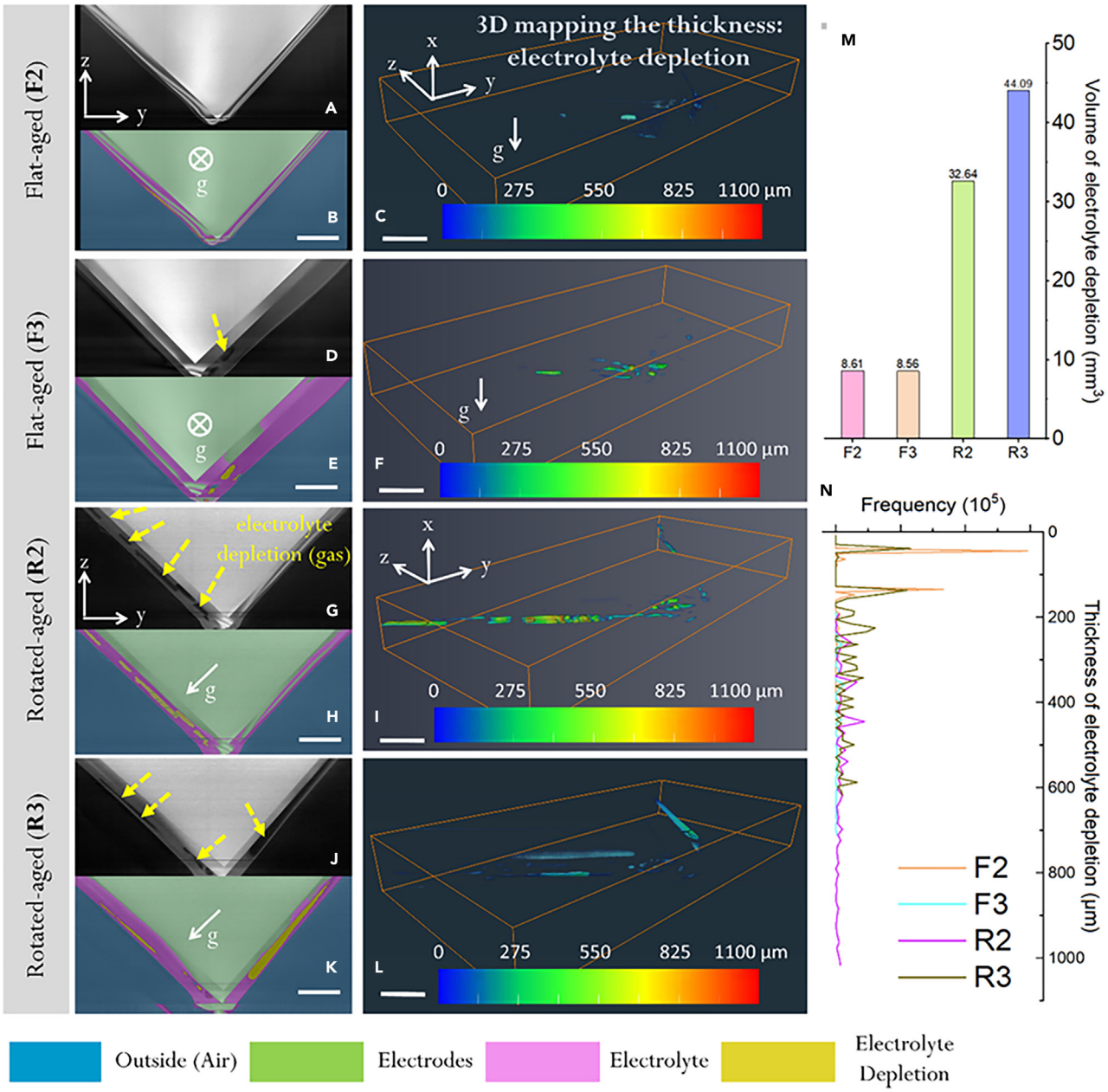

Figure 6. 3D tomographic analysis of electrolyte depletion in the aged cells

3D macrostructure of large Li-ion cells at the corner opposite to the tabs under the status of (A–C) F2, (D–F) F3, (G–I) R2, and (J–L) R3. Correspondingly, 2D front views (A, D, G, and J) are raw tomographic slices (y-z plane) selected from the same ROI volumes, and grayscale images are labeled in colors (B, E, H, and K) after deep-learning-assisted segmentation. The pink arrows also highlight the regions of electrolyte depletion. The electrolyte loss (consumption) can be rendered in 3D, coupling with their thickness mappings (C, F, I, and L). The 32 color bars represent the thickness distribution of electrolyte loss, ranging from 0 to 1,100 µm. The quantifications of electrolyte loss for both cases containing (m) the measured volumes in 3D and (n) thickness distribution. CT results provide vital evidence that the rotated-aged (R2 and R3) sample decomposed more electrolyte (generated more gas products) than that in the flat-aged (F2 and F3) sample. The scale bars represent 4 mm for (A)–(L). The color bar seen in (C), (F), (I), and (L) refers to the 3D thickness mapping of gas volume. The direction of gravity is also indicated by an arrow in (B), (E), (H), (K), (C), and (F).

misaligned distance is ~4 mm. Misalignment is a problem because it causes a reduction in surface area overlap between the electrode layers, meaning that lithium is left inactive during cycling and, in turn, causes capacity loss.[5]

More importantly, the gas formation related to electrolyte depletion was observed in both rotated-aged and flat-aged samples after aging. X-ray imaging and subsequent quantification of liquid electrolyte in this region allow for comparison of electrolyte "depletion" that can result from different displacements. The arrows identify black regions (low X-ray attenuation regions) where the electrolyte was partially decomposed, generating "pocket-like" gas products (CH_4, CO, CO_2, etc.) between the electrodes after long-term use. According to the segmented graphs, it is observed that the rotated-aged cells (R2 and R3 in Figures 5F and 5H) have a larger area of electrolyte depletion than that in the flat-aged cells (F2 and F3 in Figures 5B and 5D). This is confirmed by the volume quantification in Figure 6M, showing that the rotated-aged cell (44 mm^3) could consume electrolyte five times more than the flat-aged cell (8.56 mm^3). Also, such phenomena becomes more obvious in the 2D front view (shown later in Figures 6B, 6E, 6H, and 6K). Although these scans only cover the corner of the cells, the gas evolution in the pocket of cell suggests that there might be electrode depletion throughout the center of the cells, as displayed in the ultrasonic mapping measurements. Attempts were made to carry out CT measurements of the whole cell at a resolution sufficient to detect electrolyte depletion, but it is not possible due to the large and high aspect ratio form factor, highlighting the need for complimentary techniques, such as ultrasonic mapping, to deliver a full picture of the cause for degradation. We believe that this stresses the importance of complementary techniques because they determine different types of aging mechanisms within batteries.

In Figures 5B, 5D, 5F, and 5H, the segmentation of each cell is displayed. Using conventional segmentation approaches, such as thresholding and Otsu methods,[42] it is almost impossible to differentiate the region of electrolyte depletion (marked by yellow) from the region of outside area (marked by blue). This arises because these two regions have similar X-ray attenuation (similar grayscale values); therefore, the black regions will be classified as the same type. To distinguish these regions, a four-phase segmentation model was trained, as shown in Figure S8A; the training was completed after 43 epochs, according to the loss function (Figure S8B). The four phases are then automatically labeled in colors (blue: outside; green: electrodes and separators; pink: electrolyte; and yellow: electrolyte depletion). Although the electrode layers can be clearly identified by visual inspection, they have not been segmented separately in this study.

Similarly, 2D cross-sectional slices (front views, y-z plane) and their associated label images are demonstrated in Figure 6. A large-scale gas pockets (up to 8 mm) can be observed in the R2 sample, as shown in Figures 6G and 6H. Similar results can be found in the R3 sample (Figures 6J and 6K). This also demonstrates the importance of X-ray CT compared with other destructive methods, which are unable to observe the location of the gas products. A smaller gas pocket with a length of up to 2 mm was found (Figures 6D and 6E) in the F3 sample. Again, the rotated-aged cells underwent a higher electrolyte depletion than two flat-aged cells, and these graphs selected from the front view corroborate prior observations from the side view. The electrolyte depletion at the cell corner is difficult to be detected by ultrasonic mapping because a completely flat surface is required for this ultrasonic method.

As electrolyte depletion leads to gas generation, it is crucial to quantify the volume produced in order to understand the SoH for such a large-size, high-capacity Li-ion pouch (up to 32.5 Ah). The gas volumes via electrolyte decomposition for all samples are rendered in 3D, as shown in Figures 6C, 6F, 6I, and 6L. Here, the 3D rendered volumes of electrolyte depletion are presented for all samples, and other phases

(electrodes and external regions) are deliberately removed. The 3D graphs illustrate the distribution and thickness of the electrolyte depletion region at the cell corner. The R2 cell shows the largest thickness distribution of electrolyte depletion, ranging from 100 to 1,100 μm, whereas the F2 cell has smaller values (from 10 to 200 μm), as shown in Figure 6N. The 3D thickness mapping provides a route to visualize the geometric shape and quantify the perimeter of the electrolyte decomposition region in Li-ion pouch cells, which could be useful for future high-throughput health evaluations.

XRD measurements

In previous work and literature,[13] it is presented that the Nissan Leaf cathode contains LMO and $LiNiO_2$ (LNO). However, since then, inductively coupled plasma optical emission spectroscopy (ICP-OES) analysis of dismantled first-generation Nissan Leaf cells from the same battery pack has revealed that the cathode chemistry is LMO and NCA.[48] The results from this experiment confirm that the content ratio of LMO to NCA in the blended cathode is approximately 3:1.

The lattice parameters and weight percentage of each phase present in the cell were refined at each point measured. These synchrotron measurements were all undertaken when the cells were at the bottom of discharge (~0% SoC). Figure 7 shows the spatial variation in the lattice parameters of the cathode materials, $LiMn_2O_4$ and NCA, and the graphite *c* lattice parameter, which is directly related to the interlayer distance by c/2, across the cell. The graphite *a* lattice parameter was fixed at 2.464 Å[50] due to most of the graphite peaks being of low intensity and obscured by the other phases. The plots only cover the area of the cell where both cathode and anode sheets are present; at the edges of the cell, diffraction peaks mainly arise from the aluminum or copper tabs and the laminate pouch-cell casing, which contains aluminum and polypropylene. As can be seen in Figure 7, there are significant differences between the spatial variation in the lattice parameters between the two flat-aged cells (F2 and F3) and the rotated-aged cell (R3) that was measured. In the flat-aged cells, there is a front emanating from the top tab end of the cell, where the $LiMn_2O_4$ and NCA *a* lattice parameters are larger, spreading toward the bottom of the cell. In these two cells, the NCA *c* lattice parameter is smaller at the tab end of the cell but is larger where the front in the change in the NCA *a* lattice parameter is located. In the rotated-aged cell, the $LiMn_2O_4$ and NCA *a* lattice parameters are larger in the bottom and right side of the cell and smaller in the top left of the cell, whereas the NCA *c* lattice parameter is larger on the left side of the cell and smaller on the right side of the cell.

Pristine $LiMn_2O_4$ has an *a* lattice parameter of 8.2261(2) Å,[49] which decreases to 8.03 Å when charged to 4.5 V after going through two phase transitions.[51] With the lattice parameters for $LiMn_2O_4$ ranging from $8.2012(2) \leq a/Å \leq 8.2044(3)$ (see Table 3) the spinel material appears to be partially delithiated but still isostructural to the fully lithiated phase. The change in the lattice parameters of NCA on charging/delithiation is more complex. The *a* lattice parameter decreases from 2.865 to 2.814 Å on charging to 4.3 V, whereas the *c* lattice parameter increases from 14.244 to 14.469 Å up to 4.1 V before decreasing back to 14.394 Å at 4.3 V.[52] The lattice parameters of other layered oxide materials follow a similar trend.[53,54] Across all the cells, the NCA lattice parameters are in the region of $8.2210(3) \leq a/Å \leq 2.82370(16)$ and $14.4288(12) \leq c/Å \leq 14.4515(20)$, suggesting that the NCA phase remains highly delithiated despite the pouch cell being in a discharged state. It is assumed that changes in the lattice parameters across the cell correlate with variations in Li-content/SoC of the cathode material. In the flat-aged cells, the relithiation

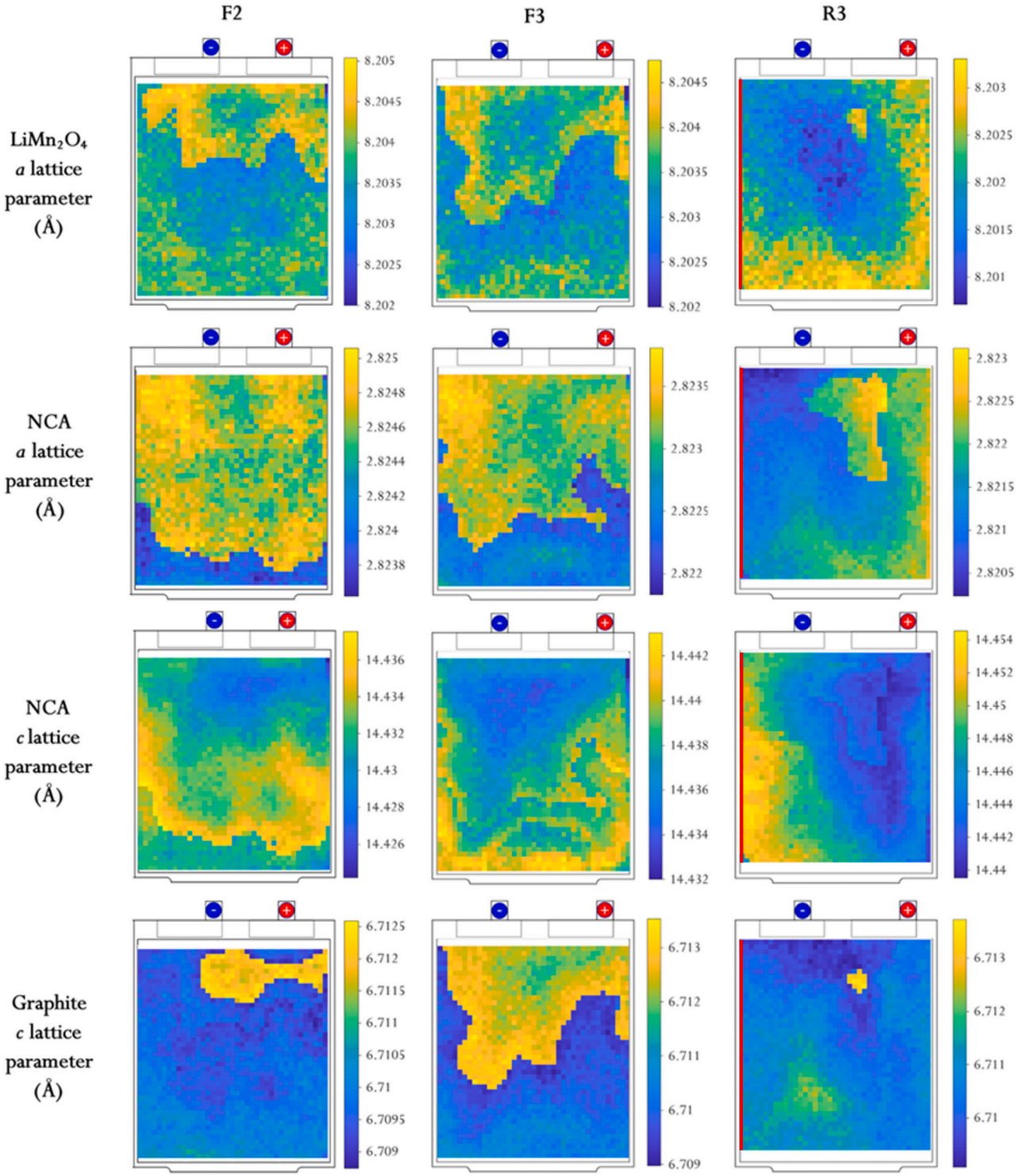

Figure 7. High-energy lateral mapping synchrotron XRD results for both the flat and rotated cells

The spatial variation in the $LiMn_2O_4$ *a* lattice parameter, NCA *a* and *c* lattice parameters, and graphite *c* lattice parameter across the two flat-aged (F2 and F3) and one rotated-aged cell (R3). The maps are overlayed onto schematics of each pouch cell to give the position, and the color bar gives the range of each refined parameter. These synchrotron measurements were all undertaken when the cells were at the bottom of discharge (~0% SoC). For rotated cells, the edges oriented upward are marked with red lines to illustrate the effect of gravity.

Table 3. The position of peaks within the distribution of lattice parameters across each cell

	F2	F3	R3
$LiMn_2O_4$ *a* lattice parameter (Å)	8.2033(3), 8.2038(3), and 8.2044(3)	8.2031(3), 8.2036(3), and 8.2040(3)	8.2012(2), 8.2018(4), and 8.2026(3)
NCA *a* lattice parameter (Å)	2.82390(15) and 2.82470(16)	2.8224(2) and 2.8232(2)	2.8210(3) and 2.8219(4)
NCA *c* lattice parameter (Å)	14.4288(12), 14.4319(12), and 14.4345(13)	14.4354(11), 14.4380(13), and 14.4403(12)	14.4428(19), 14.4479(21), and 14.4515(20)
Graphite *c* lattice parameter (Å)	6.7095(3), 6.7101(3), and 6.7121(3)	6.7100(5) and 6.7125(5)	6.7097(4), 6.7106(4), 6.7113(4), and 6.7133(3)

of the cathode material stems from the tab end of the cell and migrates toward the bottom of the cell, whereas in the rotated-aged cell, the relithiation occurs predominantly from right to left. For all cells, the negative (or anode) tab was oriented to the top left of the cell for the measurement, in keeping with the other techniques outlined in the paper. The R3 cell was aged while oriented, with the left side of the cell pointing upward and the right side of the cell pointing downward; therefore, here, relithiation is occurring at a faster rate toward the bottom of the cell. The island in the R3 cell where the NCA *a* lattice parameter is slightly larger is a cross-over point between the tab to the bottom of the cell relithiation direction favored in the flat-aged cell and the right-to-left relithiation present in the rest of the rotated-aged cell. On the anode side, there is also an area of slightly increased graphite *c* lattice parameter toward the tab end of the flat-aged cells, which is more prominent in the F3 cell. There is also a small area where the graphite *c* lattice parameter is expanded in the rotated-aged cell in a similar region to the feature in the NCA *a* lattice parameter.

Figure 8 shows a probability density estimate of the distribution in the lattice parameters across each map in Figure 7. This plot facilitates a comparison of how the average lattice parameter, or range of lattice parameters, varies from cell to cell. As can be seen from Figure 8, the variation in the lattice parameter across a map does not follow a normal distribution and tends to have several peaks. The probability density distribution generated from each map was fitted with the minimum number of Gaussian functions required to provide a reasonable fit to the distribution. The peak positions within each distribution are summarized in Table 3.

As can be seen from Table 3, there is a small decrease in the $LiMn_2O_4$ *a* lattice parameter in the F3 cell compared with the F2 cell but a substantial decrease in the $LiMn_2O_4$ *a* lattice parameter in the R3 cell. The variation in the NCA lattice parameters is more pronounced between cells; the NCA *a* lattice parameter decreases from cell F2 to F3 to R3 while the *c* lattice parameter increases. This implies that the cathode material in the R3 cell is the most delithiated, followed by the F3 cell, and then the F2 cell cathode material has the highest lithium content. If the increased state of delithiation of the cathode materials in the R3 cell is due to an overall loss in lithium inventory, then it could explain the reduced capacity measured in the R3 cell compared with the F2 and F3 cells (and the capacity of the F3 cell being slightly worse than the F2 cell). From the distribution of the graphite *c* lattice parameters, there seems to be two major phases—both within error of the standard *c* lattice parameter of graphite (6.711(4) Å) but with one phase centered around c = 6.710 Å and the other with a slightly expanded interlayer spacing ($c \sim$ 6.7123 Å). This change is too small to be from the formation of a lithiated graphite phase, such as LiC_{30},[55] although the change in lattice parameter could originate from a single layer and be averaged out across the 18 double-sided anode sheets in the cell. The ratio of these two peaks varies from cell to cell, with the F3 cell

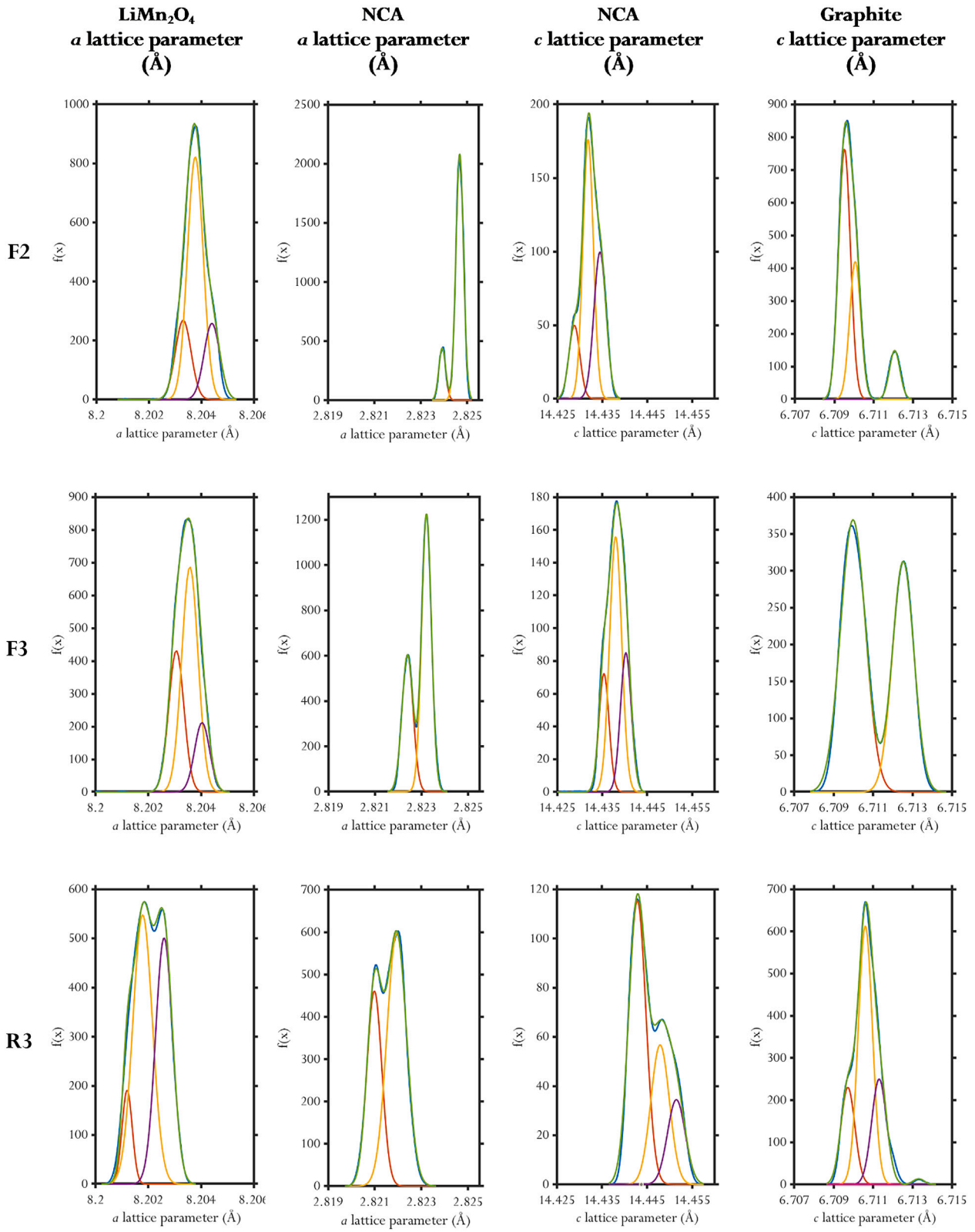

Figure 8. Probability density estimates to visualize the distribution of each lattice parameter in the flat and rotated cells

Probability density estimates to visualize the distribution in the $LiMn_2O_4$ *a* lattice parameter, NCA *a* and *c* lattice parameters, and graphite *c* lattice parameter across the two flat-aged (F2 and F3) and the rotated-aged cell (R3). Each distribution has been fitted with the minimum number of Gaussian peaks to provide a reasonable fit.

containing the most of this expanded phase and the R3 cell the least, although there is an additional small peak with an even higher *c* lattice parameter of 6.7133(3) Å. In addition to the potential presence of a small amount of intercalated lithium in some of the graphite, it is possible that in these areas, the graphite has become slightly exfoliated. *Ex situ* analysis, however, would be required to determine the exact cause of the features.

The variation in the refined weight percentage (wt %) of each phase across a cell is shown in Figure S10. Although there is some fluctuation in the proportion of each phase (e.g., ~4 wt % for $LiMn_2O_4$) across a cell, overall, the composition of the cell appears to be quite uniform. The only exception is that the cathode materials, graphite, and copper, to some extent, appear to make up a greater proportion of the cell at the top edge of the cell at the expense of the aluminum in all the cells measured. This feature could arise from the manufacturing process rather than through degradation. The spinel (LMO) comprises the major phase of the blended cathode material, being three times more abundant than the layered (NCA) oxide material.

DISCUSSION

For the first time, this paper presents a case study with multiple modalities to rationalize the understanding of the effect of cell orientation and location in a pack on its inhomogeneity, as well as provides insight into the effectiveness of different techniques for assessing the SoH of cells. This work also provides valuable information regarding state of the art of EV LIBs and acts as a benchmark for future work.

Results presented in thermal imaging, IR thermal measurements, show that the measured capacity of the flat-aged cells (F2 and F3) is higher compared with the rotated ones (R2 and R3), and the maximal SoH-based capacity difference is 2.8% (Table 1). Such a difference is not so significant, and, based on only this parameter, it could be concluded that all four cells in the battery pack aged in a similar way. However, analysis of batteries' in-plane temperature derivative maps and their hotspot positions during discharging (Video S1; Figure 3B) gave an insight into the different in-plane aging for the flat-aged and rotated-aged cells. The temperature derivative map (*dT/dt*) hotspot moves toward the cell edge that was oriented upward in the battery pack (for R2 cell to the positive tab and R3 cell to the negative tab side) in the range of 20%–60% DoD. It is hypothesized that this phenomenon can be explained by the orientation of the cell in the pack causing the area near the edge opposite to the gravity vector, on the upward side of the cells, to be less wetted by electrolyte compared with the other side battery edge. As a result, during use, the resistance (and aging) of this part of the cell will increase. Discharging from 60% to 100% DoD shows that for rotated-aged cells, hotspot movement is toward the middle of the cells. One of the reasons for this movement is that local DoD, for more aged areas, increases faster during discharging, relative to the less-aged areas. After 60% DoD, local current densities (and heat generation) can be higher for less-aged areas, leading to the hotspot movement observed.

The acoustic ultrasonic mapping method can also distinguish between the rotated and flat cells and confirms the non-uniform and greater aging in the rotated cells. These results correlate to the thermal data, which display the increased temperature under the positive tab, especially in R3, which likely caused the area of low signal attenuation (Figure 4). In R2, there is a low-amplitude section that appears in a similar place, directly under the negative tab and spread across to the edge closest to the positive tab, as the points of maximum temperature in the thermal imaging plot

(Figure 3). This increased degradation displayed using ultrasonic ToF and thermal data explains why the rotated cells have reduced SoH, albeit (2.8%), and capacity compared with the flat cells.

Since the consumption of electrolyte by the anode (graphite) is well known to be one of the most relevant degradation phenomena,[56] the level of electrolyte depletion could be seen as a health index for evaluating the cells. It is suspected that the higher acoustic attenuation is due to electrolyte depletion in the aged cells. The middle of the cell is where it is likely that most of the electrolyte has been consumed during cycling, and it follows the fact that it is this area where the signal amplitude is the lowest. All cells are aged in the middle, but the rotated cells also contain larger areas of non-uniform degradation spread away from the middle, relative to the flat cells, explaining the reduced capacity and SoH displayed in Table 1. Due to gravity, the electrolyte in the rotated cells will move to the lower section of the cell, leaving the upper section less wetted. The disparity in the amount of electrolyte covering the electrode particles in the cell will have caused increased stress and resistance while cycling. This resistance will have likely led to degradation to the internal structure and hence changes to the density and modulus of the material as well as increased non-uniform electrolyte depletion. The change will cause the signal to be dampened and attenuated relative to the pristine cell. There are no low-amplitude areas present in the center of the pristine cell because it has not been cycled and hence is not aged. It is noted that in the comparison between rotated and flat cells, it is important to recognize the role of gravity. However, it is also important to note that although gravity exerts some influence, it is unlikely to be the predominant factor contributing to battery degradation in a general context.

In addition to electrolyte consumption and unwetting, gas is produced inside the cells during cycling. This gas is produced first due to the formation of the SEI.[57] Then, as the cell is cycled and ages, further reactions with electrolyte and the internal structure of the cell will lead to further evolution.[58] Gas has a far greater acoustic impedance than solid electrode or liquid electrolyte. Therefore, the attenuation of the transmitted ultrasonic signal will be even greater since reflection and scattering in solid-gas interfaces are much more substantial than those in solid-solid or solid-liquid interfaces. This gas formation is another reason for the red, low-intensity areas seen in the ultrasound color maps (Figure 4). The rotated and flat cells are held at the same compression in the pack, meaning the generated gas would not be affected by compression differences between the two orientations. The ultrasound mapping measurements provide very similar information to the thermal imaging regarding the aging in the cells, but in a faster and easier method, highlighting its usefulness as a technique for determining SoH.

It is well recognized that the high accuracy of electrode alignment between anode and cathode can generate a homogeneous environment, including the current distribution and Li movement. However, to date, the investigation of electrode alignment in large-format pouches is limited. Herein, this paper used the corner scan by macro-CT to non-destructively inspect the 3D interior structure that can be correlated with its electrochemical performance and other techniques. Kim et al.[59] demonstrated that misaligned cells show a faster capacity fade and lower charge transfer resistance (R_{ct}) than well-aligned cells due to the irreversible loss of Li inventory within coin cells. Interestingly, similar results have been found in the large pouch cells examined here. R2 cell presents a larger electrode misalignment than the F3 cell (Figure 5). It is suspected that the rotated orientation and misaligned layers accelerate its degradation. Misalignment is a problem because it causes a reduction in surface area overlap

between the electrode layers, meaning that lithium is left inactive during cycling and, in turn, causes capacity loss. Indeed, from the electrochemical impedance spectroscopy (EIS) results of our previous study,[13] the R2 (misaligned cell) has a lower value of R_{ct} than F3 (aligned cell) in all SoCs. Furthermore, the quantitative analysis for acoustic mapping (Figure S6) suggests that the fraction of the most degraded region (gas region) in the R2 cell (24.3%) is almost double that in the F3 cell (12.6%), as depicted in Table 2. Also, the capacity retention at EoL for the R2 cell is 27.7 Ah, whereas it is 28.2 Ah for the F3 cell (Figure 2B). 2D lateral inhomogeneous aging in all battery cells was captured and identified by IR thermography (Figure 3), ultrasonic mapping (Figure 4), and HELM (Figures 7 and 8) techniques. The CT technique (Figures 5 and 6) can further interrogate the localized inhomogeneity in 3D and gain insights into the specific failure mechanisms caused by different orientations. CT confirmed the suspected results seen in the other techniques; for the rotated cells, the electrolyte depletion can be visualized in the bottom right of R2 (Figure 6). Although the CT scans only image the corner of the cell, the electrolyte depletion and gas formation seen likely spreads into center of the cell, especially for the rotated cells. The acoustic mapping appears to confirm this gas generation/electrolyte reactions in the center of the cell because of the areas of high signal attenuation. These results emphasize the importance of the correlated techniques in forensic analysis of aged cells, allowing inferences from one technique to be confirmed with additional characterization. The findings are also supported by measuring the overall resistance R in the previous work of Milojevic et al.[13] The combination of the CT and acoustic measurements to detect gassing is a good example of what is garnered from the combination of techniques. Acoustic measurements are very sensitive to changes in density (gas formation in small amounts in the porous structure) that are not resolvable with CT (especially in the center of large-format cells); however, the acoustic measurements are actually less reliable and more difficult to make at the edge of the cells, which is where the CT is best placed to image larger pockets of accumulated gas via the corner volume imaging method presented in this paper.

For the dewetted regions, due to either electrolyte dry-out or decomposition, where there is insufficient solvent to solvate Li-ions, an increased R is measured. Thus, it was expected that inhomogeneity negatively affects battery performance. The nature of rotated orientation generates an undesired electrolyte gradient. The less-wetted particles fade faster and lead to the thermal gradient, which has been detected by thermal imaging (Figure 3). The inhomogeneous electrolyte gradient could result in a non-uniform SEI film at the very beginning of cell life, which will affect the safety, durability, and rate capability.[60] This inhomogeneity is likely to be accelerated as the cell ages. Hence, it is speculated that planar electrolyte diffusion will effectively alleviate the planar heterogeneity in electrolyte distribution and electrochemical reaction. It is important to note that although the electrolyte gradient influences degradation and the location of degradation, it is not the only contributing factor. If degradation was just down to electrolyte gradient, then one side of the rotated cell would be completely degraded, and the other would not. Instead, the electrolyte gradient exacerbates the degradation process.

Suppressing inhomogeneous electrolyte depletion such as that observed in this study may require more attention from EV pack designers and manufacturers as they move toward using larger cells to achieve higher energy densities. It is also anticipated that the characterization of electrode particles at the particle level in flat and rotated cells will provide further evidence of inhomogeneity. The correlation of X-ray imaging with high flux techniques, such as hierarchical phase-contrast tomography (HiP-CT) at the European Synchrotron Radiation Facility (ESRF),[61] could

open up a new opportunity to bridge the common scale issues and advance battery development.

HELM showed a gradient in the SoC or the extent of relithiation on discharge across the cell. In the flat-aged cells, relithiation was more advanced in the cathode materials toward the tab end of the cell compared with the bottom edge and corners of the cell. This correlated with the direction of travel of the hotspots in the IR thermal imaging, with the location of the hotspots migrating from the tab toward the center of the cell on discharge. The rotated-aged cells' dT/dt_{Max} hotspots had an additional significant movement toward the side of the cell that oriented toward the upper edge, opposite to the gravity vector, after the initial movement away from the tabs. This movement is in keeping with the SoC gradient in the R3 cell, which had an area of more advanced relithiation to the left of the positive tab and the bottom of the cell. It is known that thermal inhomogeneities in cells can create a variation in local cell impedance and current density[62,63] and, in turn, cause differences in the SoC across a cell.[64] Higher current densities at the tabs of pouch cells have also been experimentally confirmed,[65] and in an *in situ* synchrotron XRD experiment on a pouch cell, the area under the positive tab was found to be of a higher SoC than the rest of the cell.[5] In a separate HELM study on a single-phase NMC622 pouch cell, Yu et al.[66] found that the edges and corners were of a lower SoC than the middle of cell. Their results are comparable to similar observations in the ultrasound maps of this paper, where the greatest aging was seen in the center of the cell. The changing orientation of the cell adds an additional factor to determining gradients in the SoC. The rotated cell may aid Li-diffusion and cause more rapid relithiation in the electrolyte-rich part of the cell compared with the dewetted region. The fact that the relatively cheap thermal imaging measurements can detect the SoC and degradation gradient displayed in expensive synchrotron experimental results is vital for the development of EoL cell testing on a large scale.

An interesting observation is the significantly higher SoC and consequently the greater state of delithiation of the NCA cathode material compared with $LiMn_2O_4$ (LMO). Using NCA in combination with LMO is thought to reduce the amount of Mn-dissolution from the spinel phase and mechanical stress in LMO during Li insertion/desertion, improving capacity retention.[67,68] However, when a blend of cathode materials is used, a compromise must be made on the voltage range. LMO is most electrochemically active above 3.9 V and finishes charging at 4.3 V, whereas NCA is more electrochemically active below 3.9 V and starts to experience accelerated fatigue above 4.05 V (vs. Li) with increased microcracking and surface modifications, such as rock-salt or spinel phase formation.[69] This will slow the rate of Li-diffusion into the NCA particles and lead to a higher charge transfer resistance. It is important to note that although previous work has seen interesting degradation phenomena linked to fatigue of cathode material at the top of charge,[5,70] it is also known that there are kinetic limitations to the re-insertion of Li at the bottom of charge,[71] so exploring the spatial variation of this via HELM at bottom of charge is indicative of kinetic degradation phenomena. Moreover, although elevated temperatures will enhance the rate of degradation of LMO and NCA, NCA is more severely affected. A prior *in situ* XRD study on a cathode material consisting of a blend of LMO, NCA, and NMC found that after cycling at 40°C, the NCA phase became electrochemically inactive with little changes in the lattice parameters on cycling and no evidence of Li insertion/deinsertion.[72] In this work on the LMO/NCA cathode blend, although there was some evidence of lithium loss from the LMO through a reduction in the *a* lattice parameter, changes in the lattice parameters of the NCA phase corresponding to delithiation were much more marked. A loss in the lithium inventory of

the cell through SEI formation can cause a shift in the anode and cathode potentials, resulting in an overcharging of the cathode material.[70] As LMO is more stable at higher voltages than NCA, any overcharging is likely to degrade NCA to a much greater extent than the LMO. This degradation may impede the relithiation of the NCA. In the HELM study, the average lattice parameters are correlated with the capacities of the cells, with the R3 cell having the lowest capacity and lattice parameters corresponding to the cathode materials being the most delithiated compared with the F2 and F3 cells. This suggests that a lower Li inventory is present in the R3 cell, as at full discharge, there is less Li present to relithiate the cathode material. From the ultrasound mapping and CT measurements, the rotated cells had a higher degree of electrolyte consumption and gas generation than the flat-aged cells, showing a more advanced level of degradation. Since gas generation can be caused by SEI formation it could thus explain the lower Li inventory in the rotated-aged cell.

Conclusions

This paper has outlined the success of using non-destructive techniques to estimate the SoH of large-size EV pouch cells. The work has shown the importance of the orientation and location of cells inside a battery pack when deciding the next use for cells at their supposed EoL. Four non-destructive techniques, IR thermography, ultrasonic acoustic mapping, X-ray CT, and synchrotron powder XRD, were used in the study. It was shown that rotated cells displayed substantially different and more severe aging patterns after their first-life usage, compared with the flat cells, after the same period of use. In contrast, a pristine cell was seen to be relatively uniform and show no discernible degradation within the cell structure. Each technique, recorded at different times, all correlated together to confirm similar results. The electrolyte gradient within the rotated cells contributed to the differing degradation observed. In the flat cells, the electrolyte was wetted uniformly, meaning that, during cycling, both electrodes had an equal covering of electrolyte and, therefore, no disparity in resistance when ions were transferred. However, the rotated cells contain less liquid electrolyte on one electrode than the other due to gravity. As the battery pack is used during EV life, the electrolyte is consumed due to aging mechanisms, leading to increased charge transfer and SEI layer resistance. This resistance is greater for the rotated cells, as one electrode will become drier sooner, leading to increased stress on the rotated cells and hence enhanced degradation. In an EV application, such electrolyte depletion cannot be ignored. The results give clear evidence to manufacturers about how to mitigate heterogeneous degradation by careful consideration of orientation effects during battery pack design.

The CT results demonstrate that deep learning-assisted segmentation tools can play a valuable role in X-ray imaging analysis. The next steps are to implement these techniques on a far greater scale with many more cells. The more expensive but more detailed X-ray techniques have been shown to confirm what was suspected by the low-cost, non-invasive IR thermography and ultrasound measurements. Therefore, there is evidence that these low-cost, non-destructive techniques alone can give accurate degradation information, allowing for a rapid decision on the cells EoL to be made, whether that be recycling, repurpose, or reuse in a second-life application such as stationary storage. Future work will apply these techniques and investigations to alternative cell formats, such as cells extracted from cylindrical-based automotive packs.

EXPERIMENTAL PROCEDURES

Resource availability

Lead contact

Further information and requests for resources and materials should be directed to and will be fulfilled by the lead contact, Professor Paul Shearing (paul.shearing@eng.ox.ac.uk)

Materials availability

This study did not generate new unique materials.

Data and code availability

The following DOIs contain the datasets and original code used in this manuscript: https://doi.org/10.5522/04/c.6868027 (X-ray computed tomography), https://doi.org/10.25405/data.ncl.24249475 (thermal imaging), https://doi.org/10.5522/04/24271045.v1 (ultrasound acoustic mapping). Further data can be made available upon reasonable request from the lead contact.

Experimental process

Thermal imaging measurement procedure

Thermal imaging measurements were conducted with a FLIR A655 thermal camera, which was calibrated for temperature range (–40°C to 150°C) with 640 × 480 pixel resolution at 1 Hz frame rate. Thermal sensitivity for the camera is less than 30 mK with a maximal error of ±2%. The surface of the cell was painted with Tetanal Camera Varnish Spray/Black paint, with a measured emissivity value of 0.96 to eliminate reflections. During measurement, the cell was placed in a bespoke holder made from Nylacast Polyacetal (POM-C) acetal solid plastic material. Aluminum plates were used to ensure a good connection between lead wires and the tabs (see Figure S2). Batteries were charged with a constant current (CC) of 50 A (*ca.* 1.5 C compared with nominal capacity) and after that held at 4.2 V constant voltage (CV) until the current dropped to less than C/20 and then left to rest for 1 h. After that, batteries were discharged at 50 A CC until the voltage reached 2.7 V (see Figure 2A). Cell cycling was performed using a BioLogic HCP-1005 potentiostat.

During discharging, cell surface temperature and capacity were measured within the environmental chamber (Binder), set to 25°C. The chamber was switched off 10 min before the end of the rest period (fan off in Figure 2A) and during thermography measurements to enable unified cell cooling conditions.

Ultrasonic mapping measurement procedure

Ultrasound mapping experiments were undertaken on the four Li-ion Nissan Leaf pouch cells used in the thermal imaging measurements as well as a pristine Nissan Leaf pouch cell, which was yet to be used inside a battery pack. The pristine cell was measured as a reference to compare with the two aged flat cells (F2 and F3) and the two aged rotated cells (R2 and R3).

The ultrasonic mapping measurements (Figure S4) were performed using an Olympus Focus PX phased array instrument (Olympus, Japan) with a 5 MHz 1D linear phased array probe consisting of 64 transducers. The transducer had an active aperture of 64 mm with an element pitch (center-to-center distance between elements) of 1 mm. The cell was covered with ultrasonic couplant (Fannin UK) prior to every scan to ensure good acoustic transmission. The transducer was moved along the length of each cell at a fixed pressure using an Olympus GLIDER 2-axis encoded scanner with the step size set at 1 mm to give a resolution of *ca.* 1 mm^2. Due to the large size of the cells, the active aperture of the

probe was wide enough to cover one-third the width, meaning that three measurements for each cell were taken and the data were combined to form the color maps.

Data from the ultrasonic signals were analyzed using FocusPC software. The waveforms recorded by the transducer were exported and plotted using custom Python code to compare how the signal changes at different points in the cell. For consistency, a specific ToF range was selected for all cells, chosen because it is where the part of the waveform, known as the "echo-peak," is located.[73] The echo-peak is useful to monitor, as it is where the waveform has traveled the whole way through the cell and reflected from the back surface, hence characterizing the entire cell. The maximum amplitude of the ultrasonic signal within this ToF range, at each point, are combined to produce a color map. The signal amplitude is a percentage proportion of 100, where 100 is the maximum intensity of the signal, meaning that the signal has been attenuated the least, as it travels through the cell, and 0 is the minimum intensity. The intensity is absolute and not normalized across all scans, meaning that an amplitude values on different cells can be directly compared. The pristine cell is a second-generation Nissan Leaf pouch, different to the first-generation aged cells of varying orientation. The authors were not able to acquire an identical first-generation pristine Nissan Leaf cell. Nonetheless, it was expected that the pristine cell would contain a uniform internal structure regardless of the specific chemistry, and this would be identified in an ultrasound map consisting of a single color (or narrow color range).

To better understand the results of the ultrasonic mapping, the areas with the highest acoustic attenuation (red area against the rest of the area in the color map) were quantified in each sample. Initially, the red green blue color model (RGB) images (Figure S5A) were converted to 8-bit images using ImageJ.[74] The area of the entire large pouch (S_{All}) was measured (Figure S5B), and the Otsu thresholding[75] was then applied to label the red region ($S_{high\text{-}attenuation}$) by referencing the associated RGB image. Next, the connected pixels were segmented as a class (Figure S5C) and measured as $S_{high\text{-}attenuation}$. Therefore, the fraction of the area with relatively high attenuation (η) can be calculated by using Equation 3.

$$\eta = \frac{S_{high-attenuation}}{S_{All}} \quad \text{(Equation 3)}$$

These results were quantified further by using the same image processing method to divide each ultrasonic map into nine sub-sections as displayed in Figure S6. For each sub-section, the percentage of highest acoustic attenuation (red region) was calculated. The calculations allowed the spatial distribution of the highly attenuating areas to be better understood.

X-ray CT and image processing

Both rotated (R2) and flat (F3) pouch samples were scanned using a lab-based X-ray CT instrument (Nikon XT 225, Nikon Metrology, UK) after the acoustic measurements. Here, corner scanning was chosen due to the large sample size (261 × 216 × 7.91 mm), high aspect ratio (length against thickness is *ca* 33), and high density of the materials (LMO and NCA). Thus, each cell was tilted 45 degrees and placed on a large plastic holder fabricated using a 3D printer (Ultimaker S3, UK). The experimental setup is displayed in Figure S7. The voltage and beam current were set at 200 kV and 150 μA, resulting in a power of 30 W. A cone-beam employing a tungsten target was used with an exposure time of 1 s per projection, and a total of 3,185 projections were collected per tomogram with a 0.5-mm Sn filter. The 2,028 × 2,028 pixels charge-coupled device (CCD) camera detector achieved a voxel resolution of 45 μm with a field of view of ca. 91 × 91 mm^2.

The raw X-ray projections were automatically reconstructed using Nikon CT Pro 3D software (version XT 4.4.4, Nikon Metrology, Tring, UK) employing a cone-beam filtered back projection algorithm. All samples were scanned under identical conditions. The reconstructed 16-bit grayscale tagged image file format (TIFF) image sequences were initially cropped to remove the exterior border and highlight the region of interest (ROI, approximately 60 × 30 × 7 mm) before importing into Dragonfly (ORS, Montreal, Canada) for subsequent image processing. The Gabor filter[76] was applied to improve the contrast of raw images before further segmentation and final 3D visualization (Avizo 2019.4, Thermo Fisher Scientific, USA). The deep learning (U-net) algorithm[77] was used to train a 3D model to identify and classify the electrodes plus current collectors (green), electrolyte (pink), gas or electrolyte depletion (yellow), and exterior air (blue) based on the grayscale, object shape, and orientation. Six ground-truth frames at multiple local regions were manually segmented to train the 3D model. Hence, four phases of U-net computational segmentation are shown in Figure S8. The profile of the training procedure, including the epochs against the loss function, is also presented in Figure S8. The trained model was then used to automatically segment the entire ROI volume. Afterward, quantification was performed to obtain the volume of electrolyte depletion and the associated 3D thickness map. More details of the thickness measurement approach can be found in Du et al.[40]

Synchrotron XRD measurement procedure

Powder XRD data were collected on three of the Nissan Leaf pouch cells on Beamline I12-JEEP[78] at Diamond Light Source. These were two pouch cells that had been flat aged (F2 and F3) and one that had been rotated aged (R3) within the battery pack. Each cell was measured one at a time in a customized holder (Figure S9), with the cell secured between two PEEK (polyether ether ketone) clamps at the top and bottom. These synchrotron measurements were all undertaken when the cells were at the bottom of discharge (~ 0% SoC). A beam energy of 67.98 keV (λ = 0.1824 Å) and beam size of 0.5 × 0.5 mm were used with a sample-detector distance of 1,055.5 mm, calibrated using a lanthanum hexaboride (LaB_6) standard. Each cell was translated in 5-mm steps both horizontally and vertically in a raster scan, starting from the top-left corner of the cell and finishing in the bottom right corner. XRD data were collected at each point with an exposure time of 5 s. Diffraction rings were imaged on a 2D Pilatus 2M CdTe detector with a 172 × 172 μm pixel size and dimensions of 1,475 × 1,679 pixels and integrated into 1D diffraction patterns using DAWN. [79] The number of points scanned by the high-energy synchrotron X-ray radiation allowed HELM across the entirety of each cell to be produced.

Rietveld refinement was performed on all of the individual diffraction patterns using the same input file (created in jEdit[80] version 5.5) with the software TOPAS version 6.[81] Diffraction peaks were observed for six phases, the aluminum and copper current collectors, the two cathode materials, $LiMn_2O_4$ and a layered oxide (refined as $LiNi_{0.8}Co_{0.15}Al_{0.05}O_2$ or NCA), graphite from the anode, and polypropylene from the laminate pouch-cell casing. For all refinements, Cu was used as an internal standard of fixed lattice parameter (a = 3.61505 Å),[82] and a sample to detector distance offset function was refined so that variations in sample thickness and sample-detector distance could be accounted for. Diffraction patterns from each cell were refined in batches, with the values of variables exported in tabulated form. These were cross-referenced with the motor positions, and the spatial variation of each parameter was plotted using MATLAB to produce a HELM plot for each cell.

SUPPLEMENTAL INFORMATION

Supplemental information can be found online at https://doi.org/10.1016/j.joule.2023.10.011.

ACKNOWLEDGMENTS

This work was part of ReLiB (https://relib.org.uk/), LiStar (https://www.listar.ac.uk/), SafeBatt (https://www.safebatt.ac.uk/), and CatMat (https://catmatproject.com/) Faraday Institution projects (grant numbers EP/S003053/1, FIRG027, FIRG014, FIRG028, and FIRG026). Diamond Light Source is acknowledged for time on Beamline I12-JEEP under proposal MG27719.

The Royal Academy of Engineering is acknowledged for the financial support of P.R. Shearing (CiET1718\59) and D.J.L.B. (RCSRF2021/13/53) under the Chair in Emerging Technologies and Research Chairs scheme. D.J.L.B. acknowledges the National Physical Laboratory (NPL) and HORIBA MIRA for the support of his RAEng Research Chair.

AUTHOR CONTRIBUTIONS

A.F., conceptualization, investigation and methodology of ultrasound mapping experiments, validation, data curation, formal analysis, visualization, writing—combining each section, writing—complete original draft, and writing—review and editing; Z.M., conceptualization, investigation and methodology of thermal imaging experiments, data curation, formal analysis, writing—thermal imaging sections, and writing—review and editing; E.G., conceptualization, investigation and methodology of HELM experiments, validation, data curation, formal analysis, writing—HELM sections, and writing—review and editing; W.D., conceptualization, investigation and methodology of X-ray CT experiments, validation, data curation, formal analysis, writing—X-ray CT and image processing sections, and writing—review and editing; R.E.O., conceptualization, investigation and methodology of ultrasound mapping experiments, writing—ultrasound mapping, and writing—review and editing; S.M., investigation and methodology of HELM experiments and writing—review and editing; P.A.C., investigation and methodology of HELM experiments and writing—review and editing; P.K.D., investigation and methodology of thermal imaging experiments and writing—review and editing; P.S.A., investigation and methodology of thermal imaging experiments and writing—review and editing; S.M.L., project administration for thermal imaging experiments, supervision, and writing—review and editing; P.K.A., project administration for HELM experiments, supervision, and writing—review and editing; P.R. Slater, project administration for HELM experiments, supervision, and writing—review and editing; P.A.A., project administration for HELM experiments, supervision, and writing—review and editing; R.J., project administration, supervision, and writing—review and editing; P.R. Shearing, project administration, supervision, and writing—review and editing; D.J.L.B., project administration, supervision, and writing—review and editing.

DECLARATION OF INTERESTS

The authors declare no competing interests.

INCLUSION AND DIVERSITY

We support inclusive, diverse, and equitable conduct of research.

Received: May 24, 2023
Revised: September 5, 2023
Accepted: October 18, 2023
Published: November 15, 2023

REFERENCES

1. Hosseinzadeh, E., Genieser, R., Worwood, D., Barai, A., Marco, J., and Jennings, P. (2018). A systematic approach for electrochemical-thermal modelling of a large format lithium-ion battery for electric vehicle application. J. Power Sources *382*, 77–94. https://doi.org/10.1016/j.jpowsour.2018.02.027.

2. Mei, W., Chen, H., Sun, J., and Wang, Q. (2019). The effect of electrode design parameters on battery performance and optimization of electrode thickness based on the electrochemical-thermal coupling model. Sustainable Energy Fuels *3*, 148–165. https://doi.org/10.1039/C8SE00503F.

3. Goutam, S., Nikolian, A., Jaguemont, J., Smekens, J., Omar, N., Van Dan Bossche, P., and Van Mierlo, J. (2017). Three-dimensional electro-thermal model of li-ion pouch cell: analysis and comparison of cell design factors and model assumptions. Appl. Therm. Eng. *126*, 796–808. https://doi.org/10.1016/j.applthermaleng.2017.07.206.

4. Yi, J., Kim, U.S., Shin, C.B., Han, T., and Park, S. (2013). Three-dimensional thermal modeling of a lithium-ion battery considering the combined effects of the electrical and thermal contact resistances between current collecting tab and lead wire. J. Electrochem. Soc. *160*, A437–A443. https://doi.org/10.1149/2.039303jes.

5. Leach, A.S., Llewellyn, A.V., Xu, C., Tan, C., Heenan, T.M.M., Dimitrijevic, A., Kleiner, K., Grey, C.P., Brett, D.J.L., Tang, C.C., et al. (2022). Spatially resolved operando synchrotron-based X-ray diffraction measurements of Ni-Rich cathodes for li-ion batteries. Front. Chem. Eng. *3*, 1–9. https://doi.org/10.3389/fceng.2021.794194.

6. Kim, G.-H., Smith, K., Lee, K.-J., Santhanagopalan, S., and Pesaran, A. (2011). Multi-domain modeling of lithium-ion batteries encompassing multi-physics in varied length scales. J. Electrochem. Soc. *158*, A955. https://doi.org/10.1149/1.3597614.

7. Veth, C., Dragicevic, D., Pfister, R., Arakkan, S., and Merten, C. (2014). 3D electro-thermal model approach for the prediction of internal state values in large-format lithium ion cells and its validation. J. Electrochem. Soc. *161*, A1943–A1952. https://doi.org/10.1149/2.1201412jes.

8. Bandhauer, T.M., Garimella, S., and Fuller, T.F. (2011). A critical review of thermal issues in lithium-ion batteries. J. Electrochem. Soc. *158*, R1. https://doi.org/10.1149/1.3515880.

9. Waldmann, T., Bisle, G., Hogg, B.-I., Stumpp, S., Danzer, M.A., Kasper, M., Axmann, P., and Wohlfahrt-Mehrens, M. (2015). Influence of cell design on temperatures and temperature gradients in lithium-ion cells: an in operando study. J. Electrochem. Soc. *162*, A921–A927. https://doi.org/10.1149/2.0561506jes.

10. Veth, C., Dragicevic, D., and Merten, C. (2014). Thermal characterizations of a large-format lithium ion cell focused on high current discharges. J. Power Sources *267*, 760–769. https://doi.org/10.1016/j.jpowsour.2014.05.139.

11. Attidekou, P.S., Milojevic, Z., Muhammad, M., Ahmeid, M., Lambert, S., and Das, P.K. (2020). Methodologies for large-size pouch lithium-ion batteries end-of-life gateway detection in the second-life application. J. Electrochem. Soc. *167*, 160534. https://doi.org/10.1149/1945-7111/abd1f1.

12. Robinson, J.B., Engebretsen, E., Finegan, D.P., Darr, J., Hinds, G., Shearing, P.R., and Brett, D.J.L. (2015). Detection of internal defects in lithium-ion batteries using lock-in thermography. ECS Electrochem. Lett. *4*, A106–A109. https://doi.org/10.1149/2.0071509eel.

13. Milojevic, Z., Attidekou, P.S., Muhammad, M., Ahmeid, M., Lambert, S., and Das, P.K. (2021). Influence of orientation on ageing of large-size pouch lithium-ion batteries during electric vehicle life. J. Power Sources *506*, 230242. https://doi.org/10.1016/j.jpowsour.2021.230242.

14. Majasan, J.O., Robinson, J.B., Owen, R.E., Maier, M., Radhakrishnan, A.N.P., Pham, M., Tranter, T.G., Zhang, Y., Shearing, P.R., and Brett, D.J.L. (2021). Recent advances in acoustic diagnostics for electrochemical power systems. J. Phys. Energy *3*, 032011. https://doi.org/10.1088/2515-7655/abfb4a.

15. Popp, H., Koller, M., Jahn, M., and Bergmann, A. (2020). Mechanical methods for state determination of lithium-Ion secondary batteries: a review. J. Energy Storage *32*, 101859. https://doi.org/10.1016/j.est.2020.101859.

16. Hsieh, A.G., Bhadra, S., Hertzberg, B.J., Gjeltema, P.J., Goy, A., Fleischer, J.W., and Steingart, D.A. (2015). Electrochemical-acoustic time of flight: in operando correlation of physical dynamics with battery charge and health. Energy Environ. Sci. *8*, 1569–1577. https://doi.org/10.1039/C5EE00111K.

17. Chang, W., Mohr, R., Kim, A., Raj, A., Davies, G., Denner, K., Park, J.H., and Steingart, D. (2020). Measuring effective stiffness of Li-ion batteries via acoustic signal processing. J. Mater. Chem. A *8*, 16624–16635. https://doi.org/10.1039/D0TA05552B.

18. Bommier, C., Chang, W., Lu, Y., Yeung, J., Davies, G., Mohr, R., Williams, M., and Steingart, D. (2020). In Operando acoustic detection of lithium metal plating in commercial LiCoO2/Graphite pouch cells. Cell Rep. Phys. Sci. *1*, 100035. https://doi.org/10.1016/j.xcrp.2020.100035.

19. Sood, B., Hendricks, C., Osterman, M., and Pecht, M. (2014). Lithium-Ion Batteries: Health Monitoring of Lithium-Ion Batteries.

20. Gold, L., Bach, T., Virsik, W., Schmitt, A., Müller, J., Staab, T.E.M., and Sextl, G. (2017). Probing lithium-ion batteries' state-of-charge using ultrasonic transmission – concept and laboratory testing. J. Power Sources *343*, 536–544. https://doi.org/10.1016/j.jpowsour.2017.01.090.

21. Robinson, J.B., Maier, M., Alster, G., Compton, T., Brett, D.J.L., and Shearing, P.R. (2019). Spatially resolved ultrasound diagnostics of Li-ion battery electrodes. Phys. Chem. Chem. Phys. *21*, 6354–6361. https://doi.org/10.1039/c8cp07098a.

22. Robinson, J.B., Owen, R.E., Kok, M.D.R., Maier, M., Majasan, J., Braglia, M., Stocker, R., Amietszajew, T., Roberts, A.J., Bhagat, R., et al. (2020). Identifying defects in li-ion cells using ultrasound acoustic measurements. J. Electrochem. Soc. *167*, 120530. https://doi.org/10.1149/1945-7111/abb174.

23. Deng, Z., Huang, Z., Shen, Y., Huang, Y., Ding, H., Luscombe, A., Johnson, M., Harlow, J.E., Gauthier, R., and Dahn, J.R. (2020). Ultrasonic scanning to observe wetting and "unwetting" in Li-ion pouch cells. Joule *4*, 2017–2029. https://doi.org/10.1016/j.joule.2020.07.014.

24. Gauthier, R., Luscombe, A., Bond, T., Bauer, M., Johnson, M., Harlow, J., Louli, A., and Dahn, J.R. (2022). How do depth of discharge, C-rate and calendar age affect capacity retention, impedance growth, the electrodes, and the electrolyte in li-ion cells? J. Electrochem. Soc *163*, 020518. https://doi.org/10.1149/1945-7111/ac4b82.

25. Chang, W., and Steingart, D. (2021). Operando 2D acoustic characterization of lithium-ion battery spatial dynamics. ACS Energy Lett. *6*, 2960–2968. https://doi.org/10.1021/acsenergylett.1c01324.

26. Bauermann, L.P., Mesquita, L.V., Bischoff, C., Drews, M., Fitz, O., Heuer, A., and Biro, D. (2020). Scanning acoustic microscopy as a non-destructive imaging tool to localize defects inside battery cells. J. Power Sources Adv. *6*, 100035. https://doi.org/10.1016/j.powera.2020.100035.

27. Wasylowski, D., Kisseler, N., Ditler, H., Sonnet, M., Fuchs, G., Ringbeck, F., and Sauer, D.U. (2022). Spatially resolving lithium-ion battery aging by open-hardware scanning acoustic imaging. J. Power Sources *521*. https://doi.org/10.1016/j.jpowsour.2021.230825.

28. Huo, H., Huang, K., Luo, W., Meng, J., Zhou, L., Deng, Z., Wen, J., Dai, Y., Huang, Z., Shen, Y., et al. (2022). Evaluating interfacial stability in solid-state pouch cells via ultrasonic imaging. ACS Energy Lett. *7*, 650–658. https://doi.org/10.1021/acsenergylett.1c02363.

29. Xie, Y., Wang, S., Li, R., Ren, D., Yi, M., Xu, C., Han, X., Lu, L., Friess, B., Offer, G., and Ouyang, M. (2022). Inhomogeneous degradation induced by lithium plating in a large-format lithium-ion battery. J. Power Sources *542*, 231753. https://doi.org/10.1016/j.jpowsour.2022.231753.

30. Heenan, T.M.M., Tan, C., Hack, J., Brett, D.J.L., and Shearing, P.R. (2019). Developments in X-ray tomography characterization for electrochemical devices. Mater. Today *31*, 69–85. https://doi.org/10.1016/j.mattod.2019.05.019.

31. Lu, X., Bertei, A., Finegan, D.P., Tan, C., Daemi, S.R., Weaving, J.S., O'Regan, K.B., Heenan, T.M.M., Hinds, G., Kendrick, E., et al. (2020). 3D microstructure design of lithium-ion battery electrodes assisted by X-ray nano-computed tomography and modelling. Nat. Commun. *11*, 2079. https://doi.org/10.1038/s41467-020-15811-x.

32. Taiwo, O.O., Paz-García, J.M., Hall, S.A., Heenan, T.M.M., Finegan, D.P., Mokso, R., Villanueva-Pérez, P., Patera, A., Brett, D.J.L., and Shearing, P.R. (2017). Microstructural degradation of silicon electrodes during lithiation observed via operando X-ray tomographic imaging. J. Power Sources *342*, 904–912. https://doi.org/10.1016/j.jpowsour.2016.12.070.

33. Zwanenburg, E.A., Williams, M.A., and Warnett, J.M. (2022). Review of high-speed imaging with lab-based x-ray computed tomography. Meas. Sci. Technol. *33*, 012003. https://doi.org/10.1088/1361-6501/ac354a.

34. Withers, P.J., Bouman, C., Carmignato, S., Cnudde, V., Grimaldi, D., Hagen, C.K., Maire, E., Manley, M., Du Plessis, A., and Stock, S.R. (2021). X-ray computed tomography. Nat. Rev. Methods Primers *1*, 18. https://doi.org/10.1038/s43586-021-00015-4.

35. Kok, M.D.R., Robinson, J.B., Weaving, J.S., Jnawali, A., Pham, M., Iacoviello, F., Brett, D.J.L., and Shearing, P.R. (2019). Virtual unrolling of spirally-wound lithium-ion cells for correlative degradation studies and predictive fault detection. Sustainable Energy Fuels *3*, 2972–2976. https://doi.org/10.1039/C9SE00500E.

36. Finegan, D.P., Scheel, M., Robinson, J.B., Tjaden, B., Hunt, I., Mason, T.J., Millichamp, J., Di Michiel, M., Offer, G.J., Hinds, G., et al. (2015). In-operando high-speed tomography of lithium-ion batteries during thermal runaway. Nat. Commun. *6*, 6924. https://doi.org/10.1038/ncomms7924.

37. Robinson, J.B., Darr, J.A., Eastwood, D.S., Hinds, G., Lee, P.D., Shearing, P.R., Taiwo, O.O., and Brett, D.J.L. (2014). Non-uniform temperature distribution in Li-ion batteries during discharge - A combined thermal imaging, X-ray micro-tomography and electrochemical impedance approach. J. Power Sources *252*, 51–57. https://doi.org/10.1016/j.jpowsour.2013.11.059.

38. Jnawali, A., Radhakrishnan, A.N.P., Kok, M.D.R., Iacoviello, F., Brett, D.J.L., and Shearing, P.R. (2022). Motion-enhancement assisted digital image correlation of lithium-ion batteries during lithiation. J. Power Sources *527*, 231150. https://doi.org/10.1016/j.jpowsour.2022.231150.

39. Bond, T., Gauthier, R., Eldesoky, A., Harlow, J., and Dahn, J.R. (2022). In situ imaging of electrode thickness growth and electrolyte depletion in single-crystal vs polycrystalline LiNixMnyCozO2/graphite pouch cells using multi-scale computed tomography. J. Electrochem. Soc. *169*, 020501. https://doi.org/10.1149/1945-7111/ac4b83.

40. Du, W., Owen, R.E., Jnawali, A., Neville, T.P., Iacoviello, F., Zhang, Z., Liatard, S., Brett, D.J.L., and Shearing, P.R. (2022). In-situ X-ray tomographic imaging study of gas and structural evolution in a commercial Li-ion pouch cell. J. Power Sources *520*, 230818. https://doi.org/10.1016/j.jpowsour.2021.230818.

41. Shateri, N., Auger, D.J., Fotouhi, A., Brighton, J., Du, W., Owen, R.E., Brett, D.J.L., and Shearing, P.R. (2022). Investigation of the effect of temperature on lithium-sulfur cell cycle life performance using system identification and X-ray tomography. Batteries & Supercaps *5*, e202200035. https://doi.org/10.1002/batt.202200035.

42. Harper, G., Sommerville, R., Kendrick, E., Driscoll, L., Slater, P., Stolkin, R., Walton, A., Christensen, P., Heidrich, O., Lambert, S., et al. (2019). Recycling lithium-ion batteries from electric vehicles. Nature *575*, 75–86. https://doi.org/10.1038/s41586-019-1682-5.

43. Hu, X., Zhang, K., Liu, K., Lin, X., Dey, S., and Onori, S. (2020). Advanced fault diagnosis for lithium-ion battery systems: a review of fault mechanisms, fault features, and diagnosis procedures. IEEE Ind. Electron. Mag. *14*, 65–91. https://doi.org/10.1109/MIE.2020.2964814.

44. Llewellyn, A.V., Matruglio, A., Brett, D.J.L., Jervis, R., and Shearing, P.R. (2020). Using in-situ laboratory and synchrotron-based x-ray diffraction for lithium-ion batteries characterization: a review on recent developments. Condens. Matter *5*, 1–28. https://doi.org/10.3390/condmat5040075.

45. Xu, C., Märker, K., Lee, J., Mahadevegowda, A., Reeves, P.J., Day, S.J., Groh, M.F., Emge, S.P., Ducati, C., Layla Mehdi, B., et al. (2021). Bulk fatigue induced by surface reconstruction in layered Ni-rich cathodes for Li-ion batteries. Nat. Mater. *20*, 84–92. https://doi.org/10.1038/s41563-020-0767-8.

46. Mattei, G.S., Li, Z., Corrao, A.A., Niu, C., Zhang, Y., Liaw, B., Dickerson, C.C., Xiao, J., Dufek, E.J., and Khalifah, P.G. (2021). High-Energy Lateral Mapping (HELM) studies of inhomogeneity and failure mechanisms in NMC622/Li pouch cells. Chem. Mater. *33*, 2378–2386. https://doi.org/10.1021/acs.chemmater.0c04537.

47. Paul, P.P., Cao, C., Thampy, V., Steinrück, H.G., Tanim, T.R., Dunlop, A.R., Trask, S.E., Jansen, A.N., Dufek, E.J., Nelson Weker, J., and Toney, M.F. (2021). Using in situ high-energy X-ray diffraction to quantify electrode behavior of Li-ion batteries from extreme fast charging. ACS Appl. Energy Mater. *4*, 11590–11598. https://doi.org/10.1021/acsaem.1c02348.

48. Gastol, D., Marshall, J., Cooper, E., Mitchell, C., Burnett, D., Song, T., Sommerville, R., Middleton, B., Crozier, M., Smith, R., et al. (2022). Reclaimed and up-cycled cathodes for lithium-ion batteries. Glob. Chall. *6*, 2200046. https://doi.org/10.1002/gch2.202200046.

49. Liu, J., Wang, X., Borkiewicz, O.J., Hu, E., Xiao, R.J., Chen, L., and Page, K. (2019). Unified view of the local cation-ordered state in inverse spinel oxides. Inorg. Chem. *58*, 14389–14402. https://doi.org/10.1021/acs.inorgchem.9b01685.

50. Trucano, P., and Chen, R. (1975). Structure of graphite by neutron diffraction. Nature *258*, 136–137. https://doi.org/10.1038/258136a0.

51. Sottmann, J., Pralong, V., Barrier, N., and Martin, C. (2019). An electrochemical cell for operando bench-top X-ray diffraction. J. Appl. Crystallogr. *52*, 485–490. https://doi.org/10.1107/S1600576719000773.

52. Zhang, N., Zhang, X., Shi, E., Zhao, S., Jiang, K., Wang, D., Wang, P., Guo, S., He, P., and Zhou, H. (2018). In situ X-ray diffraction and thermal analysis of LiNi0.8Co0.15Al0.05O2 synthesized via co-precipitation method. J. Energy Chem. *27*, 1655–1660. https://doi.org/10.1016/j.jechem.2018.06.007.

53. Märker, K., Reeves, P.J., Xu, C., Griffith, K.J., and Grey, C.P. (2019). Evolution of structure and lithium dynamics in LiNi0.8Mn0.1Co0.1O2 (NMC811) cathodes during electrochemical cycling. Chem. Mater. *31*, 2545–2554. https://doi.org/10.1021/acs.chemmater.9b00140.

54. Weber, R., Fell, C.R., Dahn, J.R., and Hy, S. (2017). Operando X-ray diffraction study of polycrystalline and single-crystal li x Ni 0.5 Mn 0.3 Co 0.2 O 2. J. Electrochem. Soc. *164*, A2992–A2999. https://doi.org/10.1149/2.0441713jes.

55. Missyul, A., Bolshakov, I., and Shpanchenko, R. (2017). XRD study of phase transformations in lithiated graphite anodes by Rietveld method. Powder Diffr. *32*, S56–S62. https://doi.org/10.1017/S0885715617000458.

56. Liu, X., Yin, L., Ren, D., Wang, L., Ren, Y., Xu, W., Lapidus, S., Wang, H., He, X., Chen, Z., et al. (2021). In situ observation of thermal-driven degradation and safety concerns of lithiated graphite anode. Nat. Commun. *12*, 4235. https://doi.org/10.1038/s41467-021-24404-1.

57. Leißing, M., Horsthemke, F., Wiemers-Meyer, S., Winter, M., Niehoff, P., and Nowak, S. (2021). The impact of the C-rate on gassing during formation of NMC622 II graphite lithium-ion battery cells. Batteries & Supercaps *4*, 1344–1350. https://doi.org/10.1002/batt.202100056.

58. Schiele, A., Breitung, B., Mazilkin, A., Schweidler, S., Janek, J., Gumbel, S., Fleischmann, S., Burakowska-Meise, E., Sommer, H., and Brezesinski, T. (2018). Silicon nanoparticles with a polymer-derived carbon shell for improved lithium-ion

batteries: investigation into volume expansion, gas evolution, and particle fracture. ACS Omega *3*, 16706–16713. https://doi.org/10.1021/acsomega.8b02541.

59. Kim, N., Byun, S., Jin, D., Dzakpasu, C.B., Park, S.H., Lee, H., Hong, S.-T., and Lee, Y.M. (2022). Electrode alignment: ignored but important design parameter in assembling coin-type full lithium-ion cells. J. Electrochem. Soc. *169*, 023502. https://doi.org/10.1149/1945-7111/ac4f23.

60. Zhang, Z., Smith, K., Jervis, R., Shearing, P.R., Miller, T.S., and Brett, D.J.L. (2020). Operando electrochemical atomic force microscopy of solid-electrolyte interphase formation on graphite anodes: the evolution of SEI morphology and mechanical properties. ACS Appl. Mater. Interfaces *12*, 35132–35141. https://doi.org/10.1021/acsami.0c11190.

61. Walsh, C.L., Tafforeau, P., Wagner, W.L., Jafree, D.J., Bellier, A., Werlein, C., Kühnel, M.P., Boller, E., Walker-Samuel, S., Robertus, J.L., et al. (2021). Imaging intact human organs with local resolution of cellular structures using hierarchical phase-contrast tomography. Nat. Methods *18*, 1532–1541. https://doi.org/10.1038/s41592-021-01317-x.

62. Mei, W., Liang, C., Sun, J., and Wang, Q. (2020). Three-dimensional layered electrochemical-thermal model for a lithium-ion pouch cell. Int. J. Energy Res. *44*, 8919–8935. https://doi.org/10.1002/er.5601.

63. Fear, C., Parmananda, M., Kabra, V., Carter, R., Love, C.T., and Mukherjee, P.P. (2021). Mechanistic underpinnings of thermal gradient induced inhomogeneity in lithium plating. Energy Storage Mater. *35*, 500–511. https://doi.org/10.1016/j.ensm.2020.11.029.

64. Fleckenstein, M., Bohlen, O., Roscher, M.A., and Bäker, B. (2011). Current density and state of charge inhomogeneities in Li-ion battery cells with LiFePO4 as cathode material due to temperature gradients. J. Power Sources *196*, 4769–4778. https://doi.org/10.1016/j.jpowsour.2011.01.043.

65. Bason, M.G., Coussens, T., Withers, M., Abel, C., Kendall, G., and Krüger, P. (2022). Non-invasive current density imaging of lithium-ion batteries. J. Power Sources *533*, 231312. https://doi.org/10.1016/j.jpowsour.2022.231312.

66. Yu, X., Feng, Z., Ren, Y., Henn, D., Wu, Z., An, K., Wu, B., Fau, C., Li, C., and Harris, S.J. (2018). Simultaneous operando measurements of the local temperature, state of charge, and strain inside a commercial lithium-ion battery pouch cell. J. Electrochem. Soc. *165*, A1578–A1585. https://doi.org/10.1149/2.1251807jes.

67. Myung, S.T., Cho, M.H., Hong, H.T., Kang, T.H., and Kim, C.S. (2005). Electrochemical evaluation of mixed oxide electrode for Li-ion secondary batteries: Li1.1Mn1.9O4 and LiNi0.8Co0.15Al0.05O2. J. Power Sources *146*, 222–225. https://doi.org/10.1016/j.jpowsour.2005.03.031.

68. Dai, Y., Cai, L., and White, R.E. (2014). Simulation and analysis of stress in a Li-ion battery with a blended LiMn2O4 and LiNi0.8Co0.15Al0. 05O2 cathode. J. Power Sources *247*, 365–376. https://doi.org/10.1016/j.jpowsour.2013.08.113.

69. Lang, M., Darma, M.S.D., Kleiner, K., Riekehr, L., Mereacre, L., Ávila Pérez, M., Liebau, V., and Ehrenberg, H. (2016). Post mortem analysis of fatigue mechanisms in LiNi0.8Co0.15Al0.05O2 – LiNi0.5Co0.2Mn0.3O2 – LiMn2O4/graphite lithium ion batteries. J. Power Sources *326*, 397–409. https://doi.org/10.1016/j.jpowsour.2016.07.010.

70. Dose, W.M., Xu, C., Grey, C.P., and De Volder, M.F.L. (2020). Effect of anode slippage on cathode cutoff potential and degradation mechanisms in Ni-Rich Li-Ion batteries. Cell Rep. Phys. Sci. *1*, 100253. https://doi.org/10.1016/j.xcrp.2020.100253.

71. Zhou, H., Xin, F., Pei, B., and Whittingham, M.S. (2019). What limits the capacity of layered oxide cathodes in lithium batteries? ACS Energy Lett. *4*, 1902–1906. https://doi.org/10.1021/acsenergylett.9b01236.

72. Darma, M.S.D., Lang, M., Kleiner, K., Mereacre, L., Liebau, V., Fauth, F., Bergfeldt, T., and Ehrenberg, H. (2016). The influence of cycling temperature and cycling rate on the phase specific degradation of a positive electrode in lithium ion batteries: a post mortem analysis. J. Power Sources *327*, 714–725. https://doi.org/10.1016/j.jpowsour.2016.07.115.

73. Owen, R.E., Robinson, J.B., Weaving, J.S., Pham, M.T.M., Tranter, T.G., Neville, T.P., Billson, D., Braglia, M., Stocker, R., Tidblad, A.A., et al. (2022). Operando ultrasonic monitoring of lithium-ion battery temperature and behaviour at different cycling rates and under drive cycle conditions. J. Electrochem. Soc. *169*, 040563. https://doi.org/10.1149/1945-7111/ac6833.

74. Schneider, C.A., Rasband, W.S., and Eliceiri, K.W. (2012). NIH Image to ImageJ: 25 years of image analysis. Nat. Methods *9*, 671–675. https://doi.org/10.1038/nmeth.2089.

75. Otsu, N., Smith, P.L., Reid, D.B., Environment, C., Palo, L., Alto, P., and Smith, P.L. (1979). Otsu_1979_otsu_method. IEEE Trans. Syst. Man. Cybern. C, 62–66.

76. Kamarainen, J. (2012). Gabor Features in Image Analysis. In Proceedings of the 3rd International Conference on Image Processing Theory, Tools and Applications, pp. 13–14.

77. Wang, R., Lei, T., Cui, R., Zhang, B., Meng, H., and Nandi, A.K. (2022). Medical image segmentation using deep learning: A survey. IET Image Process. *16*, 1243–1267. https://doi.org/10.1049/ipr2.12419.

78. Drakopoulos, M., Connolley, T., Reinhard, C., Atwood, R., Magdysyuk, O., Vo, N., Hart, M., Connor, L., Humphreys, B., Howell, G., et al. (2015). I12: the Joint Engineering, Environment and processing (JEEP) beamline at Diamond Light Source. J. Synchrotron Radiat. *22*, 828–838. https://doi.org/10.1107/S1600577515003513.

79. Filik, J., Ashton, A.W., Chang, P.C.Y., Chater, P.A., Day, S.J., Drakopoulos, M., Gerring, M.W., Hart, M.L., Magdysyuk, O.V., Michalik, S., et al. (2017). Processing two-dimensional X-ray diffraction and small-angle scattering data in DAWN 2. J. Appl. Crystallogr. *50*, 959–966. https://doi.org/10.1107/S1600576717004708.

80. Evans, J.S.O. (2010). Advanced input files & parametric quantitative analysis using topas. Mater. Sci. Forum *651*, 1–9. https://doi.org/10.4028/www.scientific.net/MSF.651.1s.

81. Coelho, A.A. (2018). TOPAS and TOPAS-Academic: an optimization program integrating computer algebra and crystallographic objects written in C++. J. Appl. Crystallogr. *51*, 210–218. https://doi.org/10.1107/S1600576718000183.

82. Otte, H.M. (1961). Lattice parameter determinations with an X-ray spectrogoniometer by the debye-Scherrer method and the effect of specimen condition. J. Appl. Phys. *32*, 1536–1546. https://doi.org/10.1063/1.1728392.